

Solar-Powered Fixed-Wing Aircraft Design

A Technical Report submitted to the Department of Mechanical and Aerospace Engineering

Presented to the Faculty of the School of Engineering and Applied Science

University of Virginia • Charlottesville, Virginia

In Partial Fulfillment of the Requirements for the Degree

Bachelor of Science, School of Engineering

Nathan Ong

Spring, 2025

Technical Project Team Members

Miles Beam

Victoria Camacho

Michael Chou

Larry Egalla

Graham Guerette

Declan Long

Christopher Recupero

James Richard

Defne Savas

Adam Snyder

Muhammad Vasal

On my honor as a University Student, I have neither given nor received unauthorized aid on this assignment as defined by the Honor Guidelines for Thesis-Related Assignments

Aldo Gargiulo, Department of Mechanical & Aerospace Engineering

Table of Contents

I. Introduction & Project Overview	4
II. Mission & Project Overview Overview	4
III. Concept of Operations	5
A. Mission Profile	5
B. Design Requirements & Constraints	6
IV. Ethical & Professional Considerations	6
V. Program Management	7
VI. Tools Utilized	7
VII. Structural Design	7
A. Design Overview & Full Aircraft CAD	7
B. Wing Design	8
1. Wing Material and Structure	8
2. Wing Shape	9
3. Airfoil Design	10
4. Structure	12
5. Winglets	14
C. Empennage	16
D. Fuselage	18
E. Landing Gear	19
VIII. Propulsion & Solar Design	21
A. Requirements and Objectives	21
B. Literature Review	21
C. Cruise Power Calculations	22
D. Solar Panel and Motor Component Selection	22
E. Propellers & Motor Casing	23
F. Simulation	24
G. Component Tests	26
H. Conclusion	27
IX. Systems Integration: Software, Avionics, & Communications Design	28
X. Aircraft Performance, Stability, and Dynamics	29
XI. Suggestions for Future Work	32
XII. Conclusion	32

XIII. Resources	33
XIV. Appendices	35
Appendix A: Functional Requirements, Operational Requirements, Mission Constr.	35
Appendix B: Team Structure Graphic	36
Appendix C: Team Budget, Proposed & Current Spendings	37
Appendix D: Airfoil comparison	39
Appendix E: Risk Management Matrices	39
Appendix F: Power Budgets	40
Appendix G: Mass Budgets	41
Appendix H: Relevant Calculations	41
Appendix I: Airfoil Wind Tunnel Test	45
Appendix J: Winglet Design Study	47

I. Introduction & Project Overview

The SPARC Team designed a high-altitude, long-duration solar-powered aircraft to address two important problems in the aerospace industry: the expensive cost of moving satellite orbits, and the polluting emissions of the rapidly growing industry.

Geosynchronous orbit (GEO) satellites are often used by militaries and governments to view one area of the world. They have become effective in surveillance, weather tracking, and communications, but they have a high barrier to use due to their high costs. GEO satellites cost around \$1 million a year to maintain, and the cost of the satellite itself and the launch resources push the total cost to over \$300 million in its lifespan of 15 years (Withington, 2020). However, a high-altitude aircraft is able to take off on short notice and be operational in most inhabited places on the planet.

The aviation industry currently accounts for over 2.5% of global CO₂ emissions and released over 1 billion tons of the greenhouse gas into the atmosphere in 2019 (Ritchie, 2024). Although greener technologies – such as hybrid electric engines and sustainable aviation fuels – exist to reduce emissions, most aircraft still use combustible fuel sources that pollute the atmosphere with harmful greenhouse gases. Some of these chemicals include carbon monoxide (CO) and nitrogen oxides (NO_x) which damage the natural ozone layer, create acid rain, and are overall detrimental to human health (Lee et al., 2021). Combustion engines also create vortex contrails that trap heat from the sun and contribute to the rising temperatures associated with climate change (Lee et al. 2021).

Solar-powered aircraft offer a potential solution to allow for long-duration surveillance missions by harnessing solar and battery technology with zero emissions. Advances in solar energy capture, lightweight materials, and innovative aerodynamic designs suggest that solar-powered aviation is feasible (Güntürkün & Çınar, 2021). However, substantial physical and technical challenges, such as the limited energy density of batteries currently prevent these technologies from scaling up to full-size, commercial applications.

This research focused on developing a solar-powered, autonomous aircraft, specifically designed for surveillance and exploration missions rather than commercial transport. By targeting an unmanned application, this project addressed a more achievable domain for solar-powered flight, since smaller, autonomous aircraft have lower power and endurance requirements. This project provides a proof of concept that will drive continued innovation in sustainable aviation technology.

II. Mission & Project Overview

The goal of this project was to design and build a **highly modular, adaptable, and autonomous** solar-powered aircraft capable of supporting a wide range of mission profiles. The aircraft's **flexible architecture** allows for the seamless integration of diverse payloads and sensors, enabling **high-endurance, continuous operation** for both military and civilian surveillance, as well as scientific and exploratory missions across varied environments. Central to the design is a modular payload bay, tailored to meet specific operational needs—ranging from environmental monitoring to communications relay—making the aircraft adaptable to current and emerging market demands.

To achieve long-duration flight, the aircraft incorporates advanced solar energy harvesting systems and efficient power storage, with the goal of sustaining multi-day or even week-long flight cycles under optimal sunlight conditions. Autonomous navigation and control systems, including GPS and autopilot capabilities, allow the aircraft to execute complex maneuvers and extended missions with minimal human oversight.

Inspired by recent advances in solar aviation, such as the Solar Impulse II and Airbus Zephyr, this project applied innovative system design methodologies and lightweight materials to create an aircraft that aligns with the mission of long-term sustainability in aerospace. In addition to meeting technical performance goals, the project aimed to serve as a platform for experiential learning, enabling undergraduate aerospace engineering students to develop expertise in the design, analysis, and integration of advanced aircraft systems. As a proof of concept, the SPARC aircraft also demonstrates the viability of current solar panels and energy storage technologies for aviation applications.

By fulfilling these objectives, the team demonstrated that undergraduate students are capable of designing and building the next generation of aircraft. Furthermore, the team contributed to the work ongoing in industry to show the practical application of solar and battery technologies in aerospace, laying a foundation for the future development of sustainable, autonomous aerial systems.

III. Concept of Operations

A. Mission Profile

The SPARC aircraft is designed to perform long-endurance, solar-powered, autonomous missions for a wide variety of surveillance and exploration purposes. Before each mission, the aircraft's onboard batteries will be fully charged via ground power while the selected payload is integrated and secured into the modular payload bay. The aircraft will then accelerate and approach rotation speed, via the support of its own landing gear, and the aircraft will transition into flight.

Following takeoff, SPARC will climb to a cruising altitude of approximately 55,000 feet using full motor power initially and transitioning to cruise climb power for efficiency. Once in cruise, the aircraft will switch to solar energy harvesting mode, using solar panels integrated into its wings to maintain propulsion and charge the batteries simultaneously. The payload equipment will operate continuously during cruise, supporting real-time data transmission via satellite communications links. Both day and night operations are planned, with batteries providing power during periods of darkness.

At the end of the mission, or upon command, SPARC will descend to a predetermined landing site. SPARC will perform a glider-style landing, initially touching down on its main landing gear onto a soft or hard surface. As the aircraft decelerates, the empennage will lower, allowing the secondary landing gear to make contact with the ground, followed by gentle contact on the landing gear positioned on the wings. After landing, the modular payload can be rapidly swapped, and the aircraft can be prepared for the next mission cycle with minimal turnaround time. A diagram of the mission operations is shown in Figure 1. Risk management analysis can be seen in Appendix E.

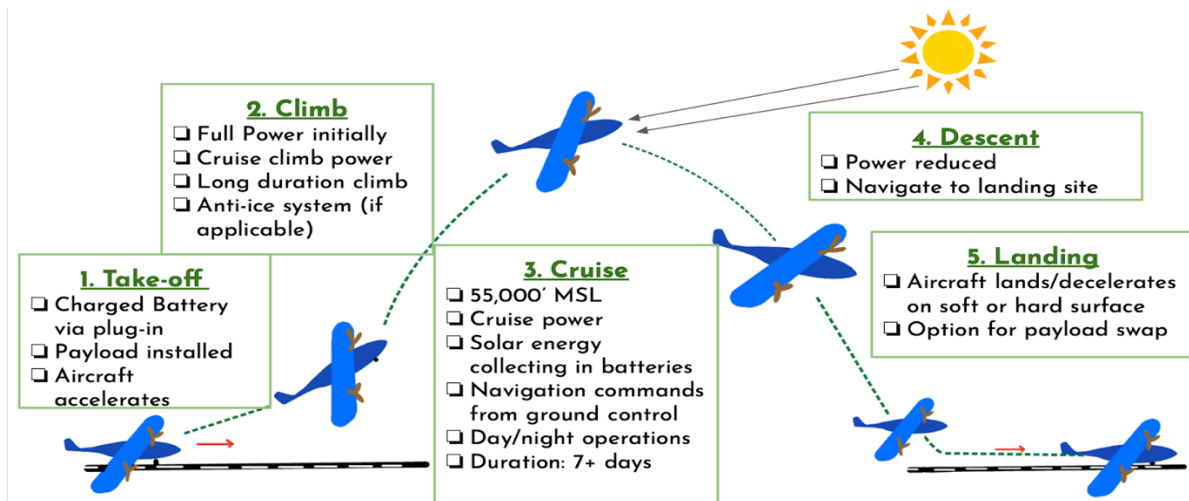


Figure 1: Mission profile for the SPARC aircraft

B. Design Requirements & Constraints

In order to design the aircraft, mission requirements and constraints were established to create expectations for the aircraft that are essential for mission success.

Functional Requirements: These were established to ensure that aircraft components are able to complete the tasks necessary for mission objectives. Functional requirements for this aircraft include aircraft aerodynamic performance, energy collection and storage, autonomous control and navigation, and data processing.

Operational Requirements: These were established to ensure that the aircraft as a whole is able to endure the range of rigors of the mission envelope. Operational requirements for this aircraft include extreme atmospheric temperature ranges, data transfer and communication at long distances to high altitudes, multi-day operation, and loss of solar charge for up to 12 hours at a time.

Mission Constraints: These were identified to ensure that the aircraft can operate and complete its mission within certain parameters. Mission constraints for this aircraft include size constraints limited by hangar size, FAA flight regulations, competitively low costs for government and large organization use, and technological limitations on solar cell and other electrical component efficiency.

The specific functional requirements, operational requirements and mission constraints determined by the group for this design are listed in Appendix A.

IV. Ethical & Professional Considerations

This capstone research project was conducted in accordance with the NSPE Code of Ethics for Engineers and the University of Virginia's Honor Code and ethical guidelines. Efforts

were made to ensure the integrity, transparency, and reproducibility of all experimental procedures and research methods.

Ethical Considerations: All data collected through experimentation has been collected meticulously to be consistent and accurate. Potential biases in data collection and analysis were also identified and addressed to ensure fairness and accuracy.

Professional Considerations: Intellectual property rights were respected by appropriately citing previous works and ensuring proper attribution. The societal implications of this work, including potential misuse and ethical deployment, were carefully considered to promote responsible innovation.

All efforts were made to uphold high ethical standards and professional integrity throughout the research process.

V. Program Management

This project was headed by Project Manager Michael Chou and Chief Engineer Miles Beam, and split into 3 subteams: Aerostructures team led by Christopher Recupero, Power team led by Graham Guerette, and Systems team led by Adam Snyder. A complete breakdown of the team structure and work completed by each subteam can be seen in Appendix B. A breakdown of the budget can be found in Appendix C.

VI. Tools Utilized

XFLR5: XFLR5, an open-source aerodynamic analysis tool based on panel methods and lifting-line theory, was extensively used throughout the SPARC project to optimize aerodynamic efficiency and ensure aircraft stability at low Reynolds numbers. The software enabled the team to iteratively refine the airfoil, wing shape, and aspect ratio to maximize lift-to-drag ratio across the full flight profile, using cruise altitude and weight as key inputs. It was also instrumental in assessing various winglet configurations and stabilizer designs. By inputting estimated masses of major components (e.g., engines, batteries, payload), the team used XFLR5 to calculate center of gravity, moments of inertia, and evaluate both static and dynamic stability. Key outputs included stability curves (e.g., C_m vs. α), L/D plots, and damping coefficients for phugoid, short period, roll, and Dutch roll modes. This iterative feedback process allowed the team to make informed design adjustments and converge on a configuration that met both efficiency and stability requirements.

Solidworks: Solidworks by Dassault Systemes was used as the computer-aided-design software (CAD). This was used for the structural designs and FEA analysis.

Physical Experiments: Physical experiments using the Low Speed Wind Tunnel, the water tunnel for PIV, and purchased solar panels were used to inform the team's design.

VII. Structural Design

A. Design Overview & Full Aircraft CAD

The full CAD assembly is shown in Figure 2. The overall design process for this aircraft was determined by considering the design constraints. Because this project was highly flexible, with no similar undertaking by an undergraduate team at UVA before, and because the students lacked prior expertise, the absence of structural constraints proved particularly challenging. The aircraft is intended to be operated in a wide range of locations, so the overall size of the design was constrained by the known size of a hanger intended to house a private jet. The wingspan was limited to 100ft to match the known size of hangers for private jets (Aviation Week Network, 2025). With this 100ft wingspan limit acting as the only size constraint, while also intending to minimize costs and maintaining an adequate area for solar panels, a wingspan of 80ft was then selected as a starting point. Due to the complexity of optimizing the wing size and the wide range of weight estimates for the aircraft components, the team kept the design with the 80 ft wingspan (although slightly extended to 81ft for the added winglets). Through the design process, the team has now calculated better estimates for the aircraft component weights, and future work can be completed to create a program for optimizing the aircraft wingspan.

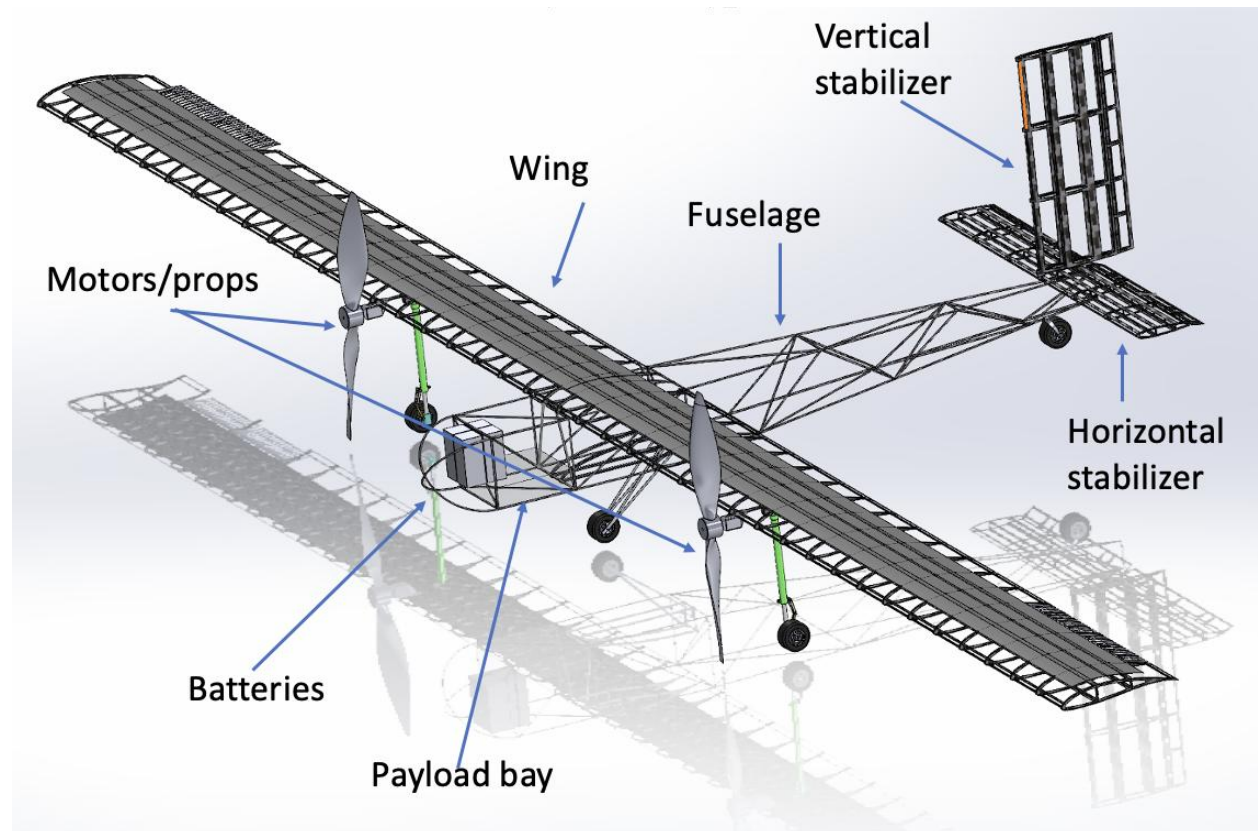


Figure 2: CAD assembly of the SPARC aircraft completed by the team

B. Wing Design

1. Wing Material and Structure

The driving factors involved in the design of the aircraft wing included manufacturing an aircraft that was structurally safe and an aircraft that minimized weight. Ashby charts were made using the GrantaEDU software package, and composite materials were shown to have the highest material parameter: $\frac{\text{yield strength}}{\text{density}}$. The Ashby chart is shown in Figure 3 and CFRP (Epoxy/HS Carbon Fiber, resin infused non-crimp fabric, UD lay-up) was shown to have the highest yield strength from the same class of materials for those materials which contained adequate information in the database. The team attempted to verify the material properties by reaching out to vendors to manufacture material samples and scaled models of aircraft components, but this proved too expensive (>\$10,000), so the online database was the only method of gathering material information. In future work, experiments with physical material components are recommended. An investigation into manufacturing methods is also recommended, although since this material is so niche, many companies keep this intellectual property out of public view. This CFRP has a yield strength of 215 Ksi on the low end of the spectrum and a density of 0.056lb/in². The cost of this material is more expensive than others at ~\$9USD/lb, however the added cost was deemed necessary due to the excellent physical material properties.

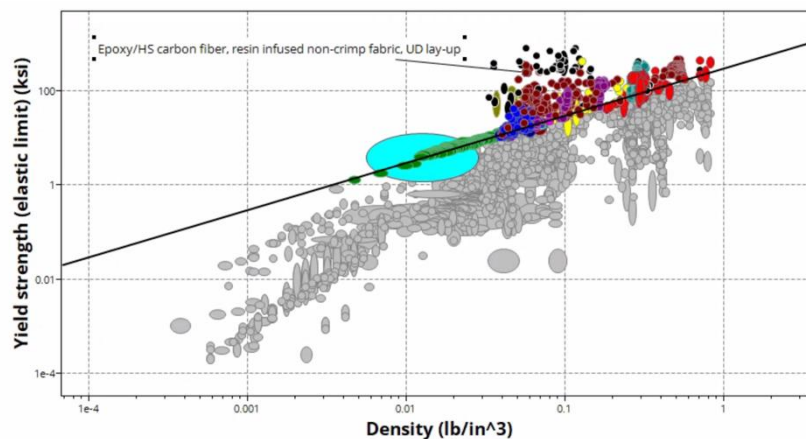


Figure 3: Ashby chart comparing yield strength vs density, depicting CFRP

2. Wing Shape

Initially, the team began iterating the wing design by utilizing a trapezoidal wing shape, with the intent that it would reduce drag and reduce the weight of the wing structure. Reducing as much weight as possible from the structure was the driving factor in this initial decision. However, when initial lift estimates showed that the trapezoidal wing shape would produce a lift force of ~570lbs (and an expected final aircraft weight greater than 570lbs), efforts were undertaken to increase the lift force. A trade study was conducted using XFLR5 software, and different wing designs were quantitatively analyzed. The parameters analyzed were the Lift force, L/D ratio, AR and usable wing area. In Figure 4, the five different wing shapes analyzed are shown along with the calculated usable wing area, mean aerodynamic chord (MAC), and aspect ratio (AR). In Figure 5, the lift at 3° AOA and the lift force is calculated at 55,000ft at 66kts for each wing shape. The cruise speed has since changed slightly for the aircraft operating

conditions, however the results of this trade study still provide insight into the comparison between the effect of the different wing shapes, which remains the same regardless of the aircraft airspeed. The rectangular wing produced significantly more lift than the trapezoidal wing, despite the decreased L/D. The increased solar area also allowed for more available electricity to power the motors and counteract the added drag created by the rectangular wing.

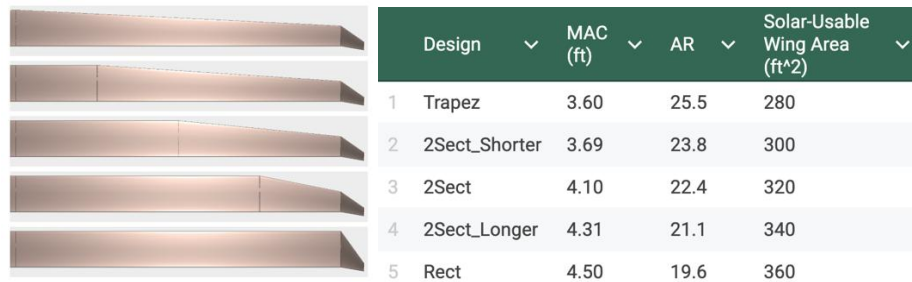


Figure 4: Five different wing shape designs with corresponding mean aerodynamic chord (MAC), aspect ratio (AR), and the solar usable wing area.

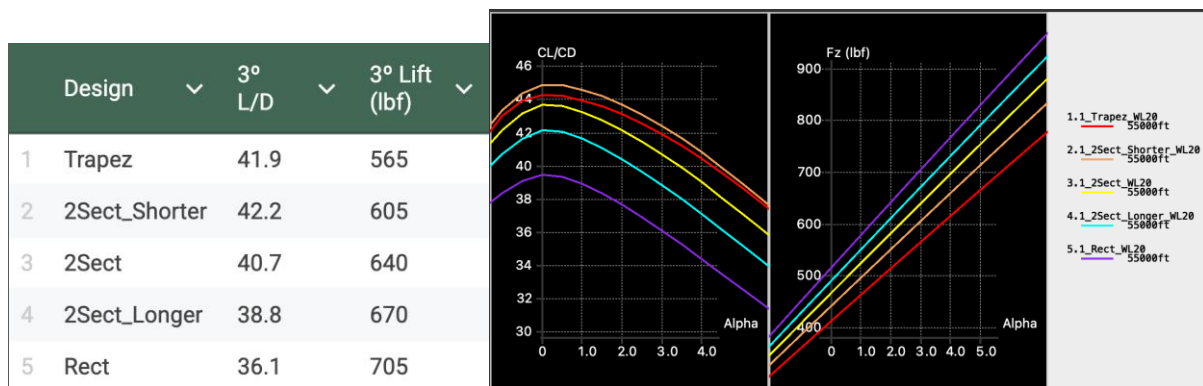


Figure 5: Five different wing shape designs with corresponding Lift/Drag ratio (L/D) and lift force.

Using the CAD model of the wing, an approximation for the density of the wing was calculated to be ~0.75lbs/ft. This calculation was completed using the chosen material for the wing (CFRP), as described in the Wing Material and Structure section. This would indicate that changing the wing shape from trapezoidal to rectangular would increase the wing weight by ~62.2lbs (28%) but would change the lift force (at 66kts) by 140lbs (25%). This net increase in lift force of ~77.8lbs along with the 28% increase in usable surface area for solar panel placement justifies the change in wing shape to rectangular. Using XFLR5, it was found that dihedral did not have a significant effect on the stability of the aircraft, although future work with higher fidelity CFD software is recommended to justify this more thoroughly. The aircraft design in this project did not include any dihedral.

3. Airfoil Design

Literature Review: The Wortmann FX 63-137 airfoil as seen in figure 6 was selected for its high lift coefficient at lower Reynolds numbers and previous use in high altitude sailplanes (Dong et al, 2018). In addition to its high performance at slower speeds, it also has “soft-stalling” characteristics where having too large of an angle of attack doesn’t lead to an immediately drastic loss of lift, as shown in Figure 7 below (Airfoiltools.com). Some comparison of the airfoils completed by using XFLR5 software can be found in Appendix D.

ANSYS Fluent software was attempted to gain a better understanding of the pressure characteristics for the FX 63-137 airfoil and verify the lift and drag coefficients. However, due to the complexity of meshing, the ANSYS fluent software was not able to converge and no reasonable lift or drag coefficients were obtained from this analysis. In order to continue moving the project forward, the team decided to pivot and perform a wind tunnel test in order to verify the lift and drag coefficients for the FX 63-137 airfoil.

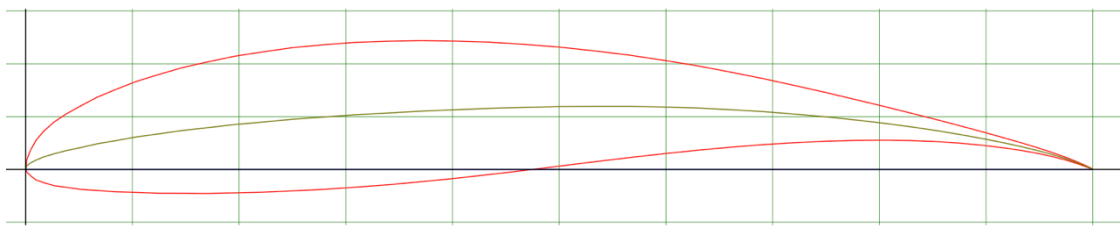


Figure 6: Wortmann FX 63-137 airfoil from airfoiltools.com

Wind Tunnel Test at Cruise Speed: The coefficient of lift vs angle of attack curve and “soft-stall” characteristics described in the literature review were experimentally tested with UVA’s wind tunnels at the aircraft’s cruise speed of approximately 72kts ~80mph

This test was conducted by running the low speed wind tunnel at UVA (Educational Wind Tunnel, Aerolab LLC, Jessup, Md) at 80 miles per hour and recording the normal and axial forces at an experimentally determined angle. Lift forces were recorded every 1 degree from -10 degrees to 18 degrees. The raw data from the experiment using an AR =1 can be found in Appendix I.

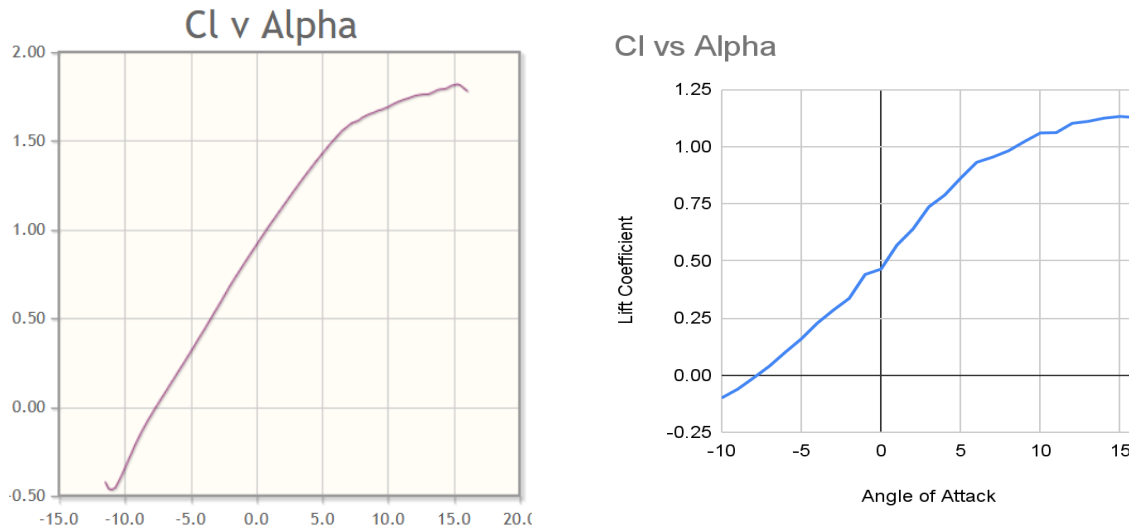


Figure 7: (Left) C_l vs Alpha curve at $Re = 500,000$ from Airfoiltools.com and (Right) C_l vs Alpha from experimental data

The theoretical C_l vs alpha curve from airfoiltools.com indicates the C_l vs alpha slope was expected to be greater than that observed in the wind tunnel. The difference was due the fact that the theoretical curve assumes an infinite wing while the experimental curve uses an aspect ratio of 1. The experimental data was not able to be directly converted to the SPARC aircraft with the AR of 19.6, because the equation to convert to an infinite wing requires an AR greater than 3. Despite this discrepancy, it is important to note the similar overall shape of the curve and the x-axis intersection point is very similar for both the theoretical and the experimental. In future tests the wind tunnel tests should be completed with a wing section with an AR of at least 3. The initial test completed by the team did not include an AR of at least 3 due to size constraints inside the wind tunnel and the driving motivator to keep the Reynolds number close to flight conditions (see Reynolds number calculations).

$$Re = \rho u L \mu \quad \text{Eq. 1}$$

529,000 for cruise, 500,000 for experimental (0.65ft chord)

The lift force was then calculated using the lift equation. This was completed for the theoretical and experimental data:

$$L = 12 C_l \rho u^2 S \quad \text{Eq. 2}$$

C_l Theoretical (AOA = 3°) = 1.3, Experimental = 0.75
Lift = 1,005 lbs Theoretical, 580 lbs Experimental

Since the weight of the aircraft is 845 lbs, the specific AOA of the aircraft can be altered in order to maintain level flight. Further experiments testing the C_l vs alpha with higher aspect ratios will need to be undertaken to examine if the theoretical more closely aligns with the

theoretical curve. If the experimental results still yield a result less than the weight of the aircraft, major structural design changes, operating velocity changes or operational altitude changes will need to be made. For the FEA calculations, the assumption was made that the lift produced would be greater than the weight of the aircraft, although future experiments will need to be made to confirm this.

4. Structure

The design for the structure of the aircraft wing was conducted in an informed, iterative manner. First, the team researched currently constructed wing structural designs, and found that the rib and spar structure is standard within industry (Abbot, 2019). The team utilized this concept due to the wealth of information available. The first analysis that was completed was the shape of the wing spars. Different wing spar shapes such as tubular, I-beam, box-structure and solid rectangular were explored. When assembling preliminary wing structures together in the CAD software (Solidworks by Dassault Systemes), it was discovered that the mass of the spar contributed significantly more to the mass of the wing than the ribs. Through the iterations completed by the aerostructures team, the spars were found to have 1.5-4x as much mass as the ribs, depending on the specific geometry of the ribs. The significantly greater mass of the spars compared to the ribs was caused by the fact that the spars stretch the entire length of the wings. It was also discovered through preliminary FEA analysis that the primary weight bearing components of the wing are the spars, while the primary structural purpose of the ribs is to form the airfoil shape and prevent buckling of the skin during moments of high bending force.

Beam theory was used in this design process. It is known that beam shapes with a high moment of inertia perform better in high bending force environments. The upwards lift force on the wing and the fixed rib at the wing root create an environment of high bending moment. Through literature review and preliminary FEA tests, the tubular and rectangular shaped wing spars did not perform as well in a high bending environment. The box-shaped wing spars have a higher moment of inertia compared to I-beams, but their greater volume (and greater mass) was not desirable as the weight of the aircraft needed to be minimized. The I beam was thus selected due to its relatively high moment of inertia and lower volume.

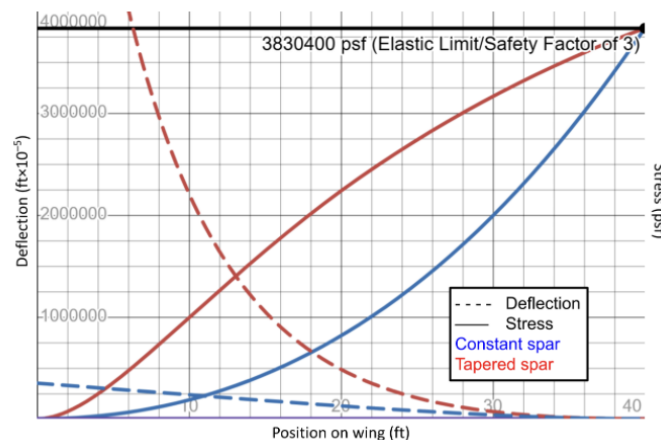


Figure 8: Constant spar size and tapered spar size deflection analysis

An analysis of the effect of incorporating a tapered spar vs a spar with constant size is shown in Figure 8. The team used beam theory and hand-calculations to complete this analysis. This analysis showed that incorporating a tapered spar significantly increases the deflection of the wing at the wing tip (0ft on the graph is located at the wing tip). Despite the increase in weight associated with the constant-sized spar, the significant decrease in deflection justifies this design decision. Different I-beam shapes were tested, and the finalized design utilizes the frame of the ribs to distribute the bending and torsional forces, as seen in Figure 9.

Originally, the wing design included 10 ribs per wing with the knowledge that the primary purpose of the ribs is to form the airfoil shape and support the weight-bearing spars. Stringers, stretching between the surface of the wings, are also commonly incorporated into aircraft wing designs to help form the shape of the airfoil. Initially, the wing designed by the group included 10 ribs and 10 stringers. However, it was found that the weight of the stringers was more than the weight of the ribs. By changing the design to have 20 ribs and only 3 stringers, this decreased the weight by around ~3lbs per wing, and still allowed for the airfoil shape to form. While this weight decrease may appear to be insignificant, any decrease in weight is preferable to allow the aircraft to satisfy the mission objective of maintaining enough power to maintain flight even with 12hrs of darkness. In Figure 9, a CAD drawing of the rib structure is shown. The design decisions were motivated by reducing as much material as possible while maintaining structural support. The spars and stringers are designed to dissipate force throughout the frame of the rib and limit stress concentrations.

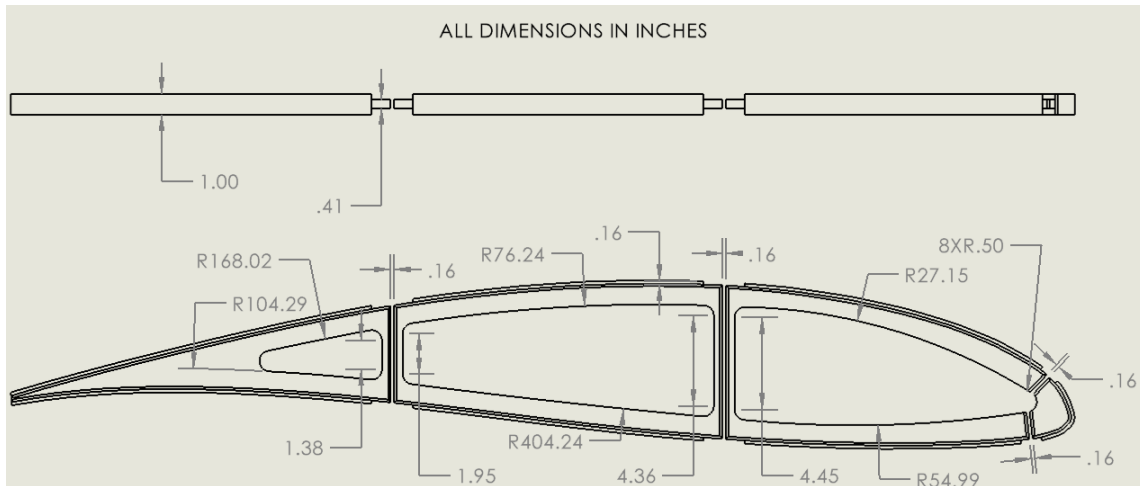


Figure 9: CAD drawing of aircraft wing rib design

In Figure 10, CAD drawings of the ailerons are shown. The SPARC aircraft uses an aileron design influenced by parameters found in literature. In literature it was found some ailerons are designed at around ~9% of the wing area and ~20% of the chord length (Diehl, 1923). Modern jet airliners have aileron sizes less than the 9% wing area. Since the SPARC aircraft is designed to operate within environments where quick maneuvers are not necessary or desired. Slow rolling

capabilities to turn the aircraft satisfy the mission requirements, since most of the time, the aircraft will operate in steady cruise flight. The ailerons of the SPARC aircraft are around ~5% of the total wing area.

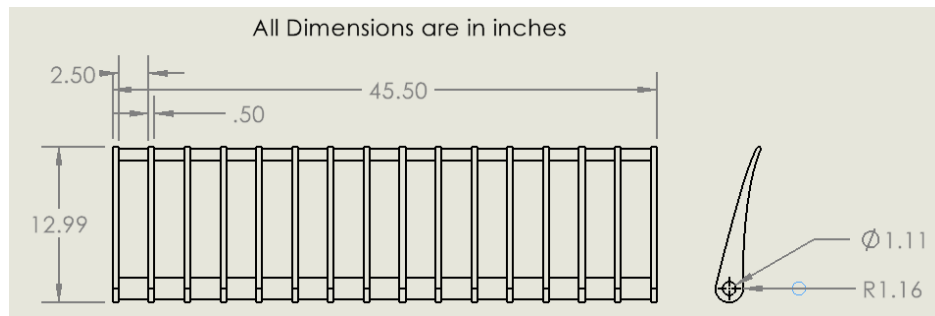


Figure 10: CAD drawing of aircraft wing aileron design

5. Winglets

Background & Introduction: To evaluate the impact of different winglet designs on the wingtip vortices, Particle Image Velocimetry (PIV) was performed using the water tunnel in the MAE building. The goal of this experiment was to find the optimal winglet configuration in both shape and winglet cant angle to improve the aerodynamic efficiency of the SPARC aircraft. (list of winglet designs in appendix J).

Wingtip vortices are generated in air as the high-pressure region rises above the wingtip to the low-pressure region, creating rotating vortices. The vortices increase downwash and induced drag on the aircraft. Winglets improve aerodynamic efficiency by reducing vortex strength and induced drag by preventing high-pressure air from spilling over the wingtip, as well as reducing downwash, making the total lift vector more vertical.

To test this experimentally, the team 3D printed each winglet design, attached it inside the water tunnel and performed PIV for each design at a 15° angle of attack. PIV is a technique used to visualize and measure fluid flow by tracking the movement of tiny particles seeded into the fluid. A laser sheet illuminates the particles, and high-speed cameras capture successive images of their positions over time. By analyzing the displacement of particles between images, the velocity and direction of the fluid flow can be calculated. The images were captured at approximately 0.10 chord lengths downstream of the airfoil in an orientation perpendicular to the vortex axis, as well as a configuration parallel to the vortex axis showing the effect of the vortex from the wing's trailing edge to approximately 8 chord lengths downstream. Post-processing and analysis were performed using PIVlab on the MATLAB application. Raw images and data can be found in Appendix J.

The experiment is constrained by Reynolds number, as the water tunnel has a max freestream velocity of 0.04 m/s. The resulting maximum Reynolds number is about 30,000 compared to the cruise Reynolds number of ~500,000. While the wingtip vortices do not perfectly scale from low to high Reynolds number, the basic structure and general trends will still carry over, making the experiment an accurate representation.

The analysis was conducted using the fundamental characteristics of wingtip vortices. Values for circulation (Γ), vorticity, vortex core radius, downwash strength, and vortex decay

rate were analyzed using PIVlab to form conclusions about the optimal winglet design. For more information on each metric and how they were calculated, see Appendix J. The basis for the conclusion at the end of this section lies in the following analysis.

Circulation: For this analysis, circulation was calculated at a fixed radius of 3.77 mm from the vortex core for consistency across all winglet designs. The resulting values were then ranked from highest to lowest, as shown in Table J1 of Appendix J. As expected, the baseline wing exhibited the highest circulation, measured at $-0.00025 \text{ m}^2/\text{s}$, indicating the strongest and least efficient vortex. The lowest circulation, and therefore the most favorable in terms of vortex attenuation, was observed with the Blended Up winglet, at $-0.000072 \text{ m}^2/\text{s}$. Closely following was the Blended Down winglet, with a circulation of $-0.000098 \text{ m}^2/\text{s}$, making both designs strong candidates for reducing induced drag.

Vorticity and Downwash: Both vorticity and downwash were extracted from the PIV data. Mean downwash was calculated as the average vertical velocity component over a defined area encompassing the vortex, and mean vorticity was averaged over the same region. Analysis of the results showed that the baseline wing produced the strongest vortex and most negative downwash, indicating the least efficient configuration—as expected. In contrast, the Back-Curved winglet demonstrated a strong balance, with moderate vorticity and the lowest (slightly positive) mean downwash at $7.67 \times 10^{-5} \text{ m/s}$, suggesting minimal induced drag. The Blended Down winglet produced the weakest vortex overall, along with a relatively low downwash, making it another high-performing configuration.

Overall, while the Blended Down winglet generated the lowest vortex strength, the Back-curved winglet’s combination of weaker vortex intensity and minimal downwash suggests it may offer superior induced drag reduction and thus the most aerodynamic benefit.

Core Radius: As shown in Table J3 of Appendix J, the baseline wing unexpectedly produced the largest core radius of 11.30 mm, while the Blended Down winglet produced the smallest core at 6.02 mm. Although this initially seemed counterintuitive—given the expectation that winglets would diffuse the vortex and expand the core—further analysis revealed that the baseline vortex, while larger, was also stronger and more persistent, resulting in a wider and more energetic core.

Conversely, winglets reduced vortex strength, leading to smaller, weaker, and more compact cores. As expected, aside from the baseline wing which produced large velocities, each winglet produced relatively similar small velocity gradients. Based on a balance of core size and reduced vortex strength, the Back-Curved winglet appears to offer the most favorable performance in terms of minimizing induced drag through vortex attenuation. This winglet had the largest radius with a relatively small velocity gradient.

Decay Rate: Table J4 of Appendix J gives a comparison of the fitted decay constants for each winglet type. The baseline wing had the lowest decay rate, with a constant of approximately 0.035, while the blended down winglet had the highest decay constant of 23.44. All winglet-equipped configurations demonstrated significantly higher decay constants. These values indicate that winglets substantially increase the rate at which trailing vortices dissipate.

These results suggest that the addition of winglets effectively weakens the strength and persistence of wingtip vortices by enhancing their decay, and should be implemented on the SPARC aircraft to improve aerodynamic efficiency. Among the tested winglets, the blended down configuration showed the highest decay rate, suggesting it may be the most effective design for minimizing vortex-induced performance losses.

Winglet Study Conclusion: Based on the comprehensive analysis of circulation, vorticity, downwash, vortex core radius, and decay rate, the Back-Curved winglet emerges as the most balanced and effective design for reducing wingtip vortex strength and minimizing induced drag. While the Blended Down winglet demonstrated the lowest circulation and highest vortex decay rate—indicating strong performance in attenuating vortex intensity—the Back-Curved configuration consistently performed well across multiple criteria. It combined moderate circulation and vorticity with the lowest (and slightly positive) mean downwash, and exhibited a relatively large vortex core radius with low velocity gradients, all of which point to improved aerodynamic efficiency. Though the Blended Down winglet showed the fastest vortex dissipation, its smaller core and slightly higher downwash suggest a marginally less favorable aerodynamic profile compared to the Back-curved design. Therefore, the Back-Curved winglet is recommended as the optimal configuration for SPARC, offering the best overall reduction in vortex-induced performance losses while maintaining favorable aerodynamic characteristics.

C. Empennage

The empennage of the aircraft was designed in a traditional T-tail structure. The group initially proposed various designs including a V-tail design and a T-tail design which included half of the vertical stabilizer below the fuselage and half above the fuselage. The group decided to move forward with the traditional T-tail structure due to the simplicity of the flight control surfaces (elevator and rudder), and the relative ease of integration into the fuselage structure. The size of the empennage was iterated throughout the project in collaboration with the fuselage, in order to satisfy the necessary vertical and horizontal stabilizer coefficients. The airfoil chosen for the vertical stabilizer and the horizontal stabilizer was NACA 0012 since it is symmetrical and symmetrical airfoils are best suited for this purpose (NASA Glenn Research Center). In future work, different symmetric airfoils should be compared to find airfoil with the least drag

The vertical stabilizer design was influenced by the vertical stabilizer volume equation where V_v is the vertical tail volume coefficient, S_v is the area of the vertical tail, L_v is the distance from the aircraft in the center of gravity to the aerodynamic center of the vertical tail, S_w is the area of the aircraft wings and b is the wingspan of the aircraft:

$$V_v = \frac{S_v L_v}{S_w b} \quad \text{Eq. 3}$$

Gliders are the most comparable aircraft type to the SPARC aircraft and they should have a V_v of around 0.02 (Blaesser and Frederick). The L_v for the aircraft with the most updated aircraft design at the time of the finalized design of the empennage is 20ft. The S_w is 360ft², and the b is ~81ft. In order to obtain a V_v of 0.02, S_v was calculated to be 29.42ft², with a chord

length of 45.07in and a height of 94in. The design of the vertical tail was kept rectangular for simplicity. The CAD drawing of the vertical tail is shown in Figure 11.

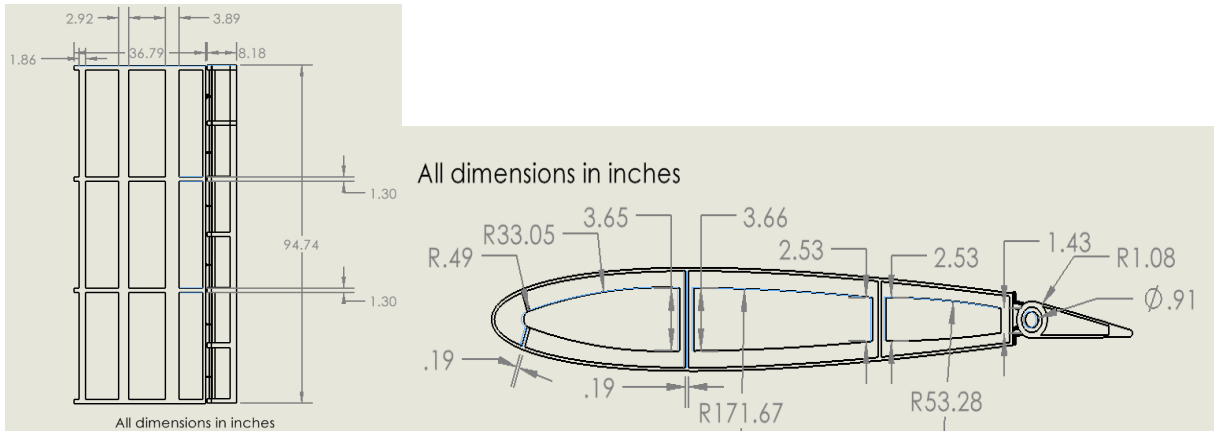


Figure 11: CAD drawing of aircraft vertical tail design

The horizontal stabilizer was designed in a similar manner as the vertical stabilizer. The horizontal stabilizer volume coefficient, H_v is dependent on the the surface area of the horizontal stabilizer – S_H , the distance from the center of gravity to the aerodynamic center of the horizontal stabilizer – L_H , the surface area of the wing – S_w , and the mean aerodynamic chord – C_{mac} .

$$H_v = \frac{S_H L_H}{S_w C_{mac}} \quad \text{Eq. 4}$$

An H_v for gliders, a comparable aircraft type, are known to be around 0.5 . With an L_H of ~20ft, the same as the L_V for the vertical stabilizer, S_w at 360ft², C_{mac} at 4.5ft. The S_H was calculated to be 41.2ft² to satisfy the $H_v = 0.5$ requirement. The chord length was calculated to be 31.48in and the horizontal stabilizer length was calculated to be 188.5in. The CAD drawing of half of the horizontal tail is shown in Figure 12.

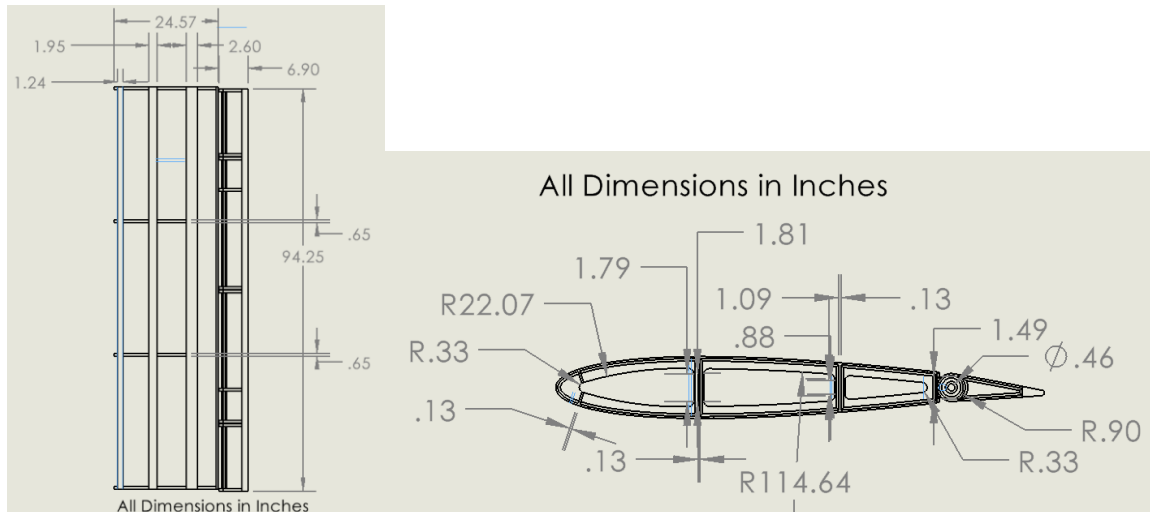


Figure 12: CAD drawing of aircraft horizontal stabilizer (half) design

D. Fuselage

The first iteration of the fuselage was inspired by the default fuselage used during the XFLR5 simulations. After having run simulations to find the ideal wing and empennage locations, it was determined that it would be the best course of action to import this fuselage into CAD software. Since XFLR5 had created the shell, the team worked backwards and made preliminary designs of the internal structure, opting for a plate and stringer design. However, after completion of the first iterations it was determined that the complex design and irregularly shaped stringers would make manufacturing too difficult.

The second iteration of the fuselage was a triangular truss design, similar to that of the Solar Impulse II. The fuselage had a larger section under the main wing to support the batteries and payload bay, and then gradually shifted into a narrower section that supported the empennage. After this truss was completed, FEA simulations were run in Solidworks with estimated wing loads placed at empennage attachment point. These simulations provided useful feedback and showed that a significant portion of the truss members were experiencing minimal load compared to others, and could be removed from the design to save weight for later iterations.

For the final iteration, moment of inertia calculations suggested a rectangular cross section would be more effective at resisting bending in comparison to a triangular cross section. Approximating the fuselage structure as a shell, where all of the volume is located at the perimeter, the ratio (R) of moment of inertia-to-volume for a rectangle compared to a triangle as a function of its height (h) is shown in Figure 13. The full calculation is displayed in appendix H.

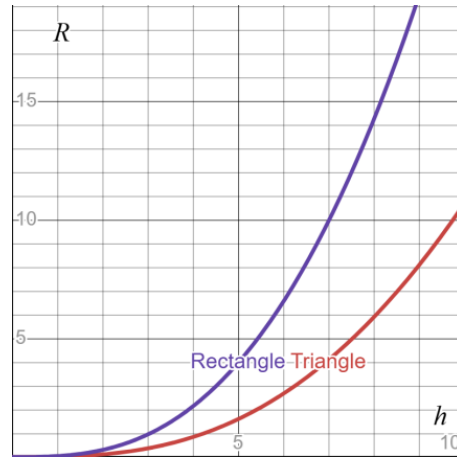


Figure 13: R vs. h for a rectangular and triangular cross section

With the team abandoning a more streamlined shape in favor of simpler design iteration and cheaper manufacturing, prior literature suggests that a Warren truss is optimal for a rectangular cross section truss-shaped fuselage. Its alternating interior members distribute the load from tip to tail with minimal volume. Like previous iterations, FEA was run to iteratively reduce the thickness of each member until an optimal volume was found.

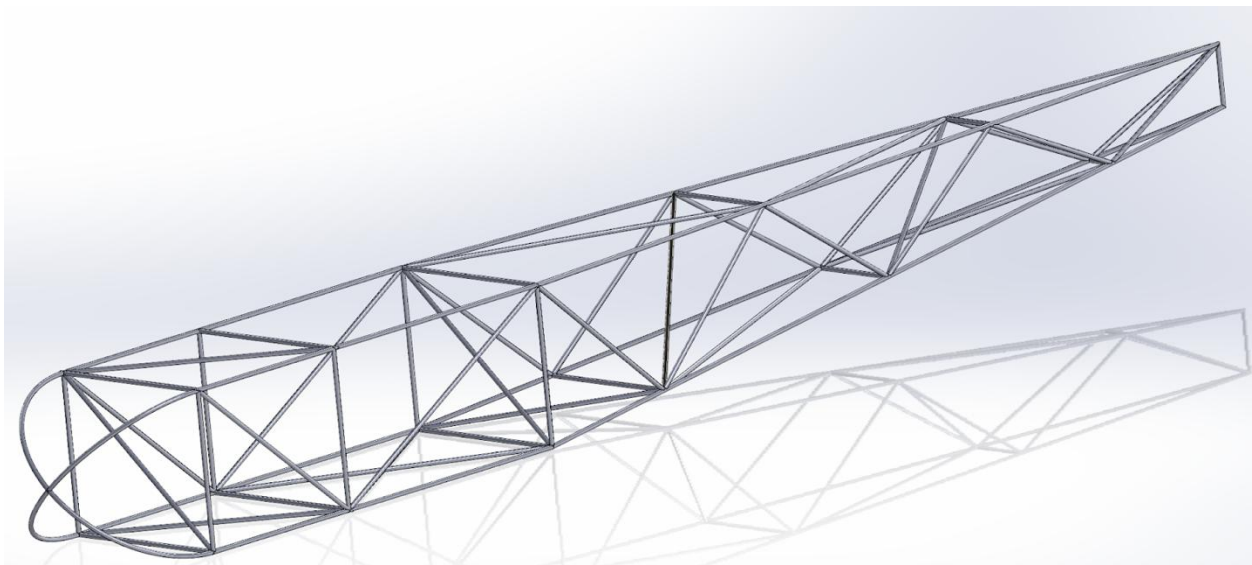


Figure 14: Warren truss fuselage with aerodynamic nose

E. Landing Gear

Two landing gear designs had to be developed for the SPARC: the main landing load-bearer under the fuselage and two landing gears under each wing's engines for stability and accounting for bending in the wings. Both landing gears were designed to be retractable rather than fixed, aiming to reduce drag when the landing gear is not in use. A smaller wheel is also

fixed close to the craft's tail and is used for empennage support during landing when the aircraft decelerates sufficiently.

Initially, the landing gear design process involved evaluating various concepts, such as fixed, shaft-suspension-based, and retractable systems, before selecting the final approach. The first landing gear design made in CAD was a shaft-suspension model, designed to account for a wide range of loads possible as the loads of the plane were not yet known. As this design neared completion, the decision was made to switch to a less obtrusive design as more factors became clear. There was no need for a complex design as the weight of the plane was far below a heavier aircraft which utilizes the shaft-suspension model. Instead, a simpler retractable design was designed. The winged landing gear, to allow for retractability, would have to be foldable as the vertical location of the wings required this mechanism to be vertically tall. The first shaft-suspension design was partially recycled to create the foldable design.

The main landing gear requires a single push/pull actuator for functionality, directly pushing the plate connected to the wheel around a rotating joint to create a circular motion with the wheel attached to the end of it. When pushed, the wheel rotates below the fuselage, and when contracted, it disappears back into the fuselage and the top of its rotation. The integration into the fuselage is done using the front and back of the design's holes as a collar that fit the truss members, directly placing the landing gear onto the aircraft's truss for structural integrity. Below in Figure 15 is the landing gear fully extended.



Figure 15: Landing gear design

The folding landing gear maintains the shaft-suspension design as initially conceptualized, with reductions to the diameter of the shaft and an increase in shaft length to account for the increased vertical requirement and smaller intended load. Whenever there is a load on the end of the wheel, the linkage from the joint piece at the bottom and the upper shaft allows a suspension effect for whatever variable load the wheel feels. The folding of the landing gear is managed entirely by a revolving trunnion powered by a rotary actuator within the wing integration. A maximum of 100° of rotation is allowed from the rotary actuator starting from the winged horizontal down towards the ground to allow a fully folded and vertically straight configuration as required. Integration is simple as the shaft is only connected to the wing via the revolving trunnion. The extended landing gear is shown in Figure 16.

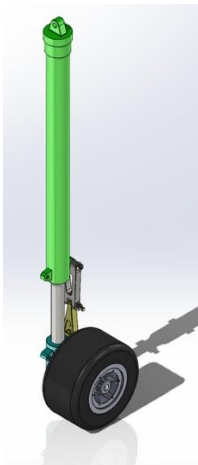


Figure 16: Folding landing gear fully extended

The final component is a simple wheel attached to an arm on the tail of the aircraft, with two main goals. It stops the back end of the aircraft from coming into contact with the ground, and is strong enough to support the intended landing maneuver for the aircraft, coming down tail first and rotating the rest of the plane to be in line with the ground soon afterwards.

All wheels used were modeled after that of the Cessna Skyhawk 172 for a consistent, low-weight design. The tires were designed of rubber, with the inner rimming of the tires and the landing gear itself made of carbon fiber for ample strength and once again low-weight. The tires themselves are joined to each landing gear by being concentrically fitted onto a shaft through their axle. The tires are only able to roll forward and backward respective to the aircraft to avoid unintended and unnecessary movements.

VIII. Propulsion & Solar Design

A. Requirements and Objectives

The requirements and objectives of the propulsion and solar design were to generate, via an onboard solar array, the necessary cruise power for daytime operation and, assuming a perfect 12 hours of sunlight and 12 hours of darkness, to simultaneously supply equal usable power to batteries of adequate capacity for nighttime use. The aircraft also needed to be capable of generating necessary power for a rate of climb of 300 ft min^{-1} from ground to an altitude of 55,000 feet and to supply power for constant communication, payload, and avionics control. The power budget can be found in Appendix F

B. Literature Review

A review of previous theory on long endurance solar aircraft was conducted. The propulsion design was informed firstly by the 2011 Colloquium Lecture, “Fly Forever,” by NASA Langley Research Center’s (LaRC) System Analysis Branch. This presentation details the power required for steady state cruise of an aerial vehicle:

$$P_{cruise} = \frac{1}{2} \rho V^3 C_D S_{ref} \quad \text{Eq. 5}$$

Where ρ is air density, V is aircraft velocity, C_D is the coefficient of drag, and S_{ref} is the reference wing area. This relationship is useful for determining cruise power given a required cruise velocity. The LaRC presentation goes on to require that lift at cruise equal weight of the aircraft via the following relationship:

$$Weight = \frac{1}{2} \rho V^2 C_L S_{ref} \quad \text{Eq. 6}$$

where C_L is the aircraft coefficient of lift at a cruise angle of attack. Given the mission objective to prioritize endurance and modularity over speed or maneuverability, cruise velocity was not a limiting parameter. As such, Equations 1 and 2 were combined to yield a relationship between cruise power and aircraft parameters which did not depend on cruise velocity:

$$P_{cruise} = \frac{C_D}{C_L^{1.5}} \sqrt{\frac{2ARg^3}{\rho}} \cdot \frac{m^{1.5}}{b} \quad \text{Eq. 7}$$

where aspect ratio AR and wingspan b serve as an equivalent expression for S_{ref} . Equation 3 was verified by the work of Alsahlani et al., who further refine a total power requirement with component efficiencies and avionics and payload power supply:

$$P_{total} = \frac{1}{\eta_{controls} \eta_{motor} \eta_{gearbox} \eta_{propellor}} \cdot P_{cruise} + \eta_{converter} (P_{avionics} + P_{payload}) \quad \text{Eq. 8}$$

where $\eta_{controls} \eta_{motor} \eta_{gearbox} \eta_{propellor}$ represents the combined powertrain efficiency

C. Cruise Power Calculations

Substituting values from the results of the structural design into Equation 7 yielded a required P_{cruise} of 2.44 kW constant output by the propulsion system. Power supply to the avionics system and the payload bay were treated as negligible for the conceptual design phase. To compensate, and based on typical glider efficiency reports (Deutsch et al.), a conservative combined powertrain efficiency of 0.5 was subbed into Equation 4, resulting in a P_{total} value of 6.62 kW required as constant supply to the propulsion system.

The required battery mass and solar panel area can then be calculated, given an operational period of 24 hours with a hypothetical 12 hours of full sunlight and 12 hours of full darkness. The battery mass is calculated using:

$$m_{battery} = \frac{t_{op} P_{total}}{e_{battery}} \quad \text{Eq. 9}$$

where t_{op} is the operational time on pure battery power, 12 hours in this case, and $e_{battery}$ is the energy density of the lithium ion battery, taken to be approximately 330 W-h/kg. This results in a theoretical battery mass of 240.7 kg.

D. Solar Panel and Motor Component Selection

Two 3500-watt brushless DC motors were selected for the propulsion system based on power calculations. Brushless DC motors are commonly used in electric vehicles due to their high efficiency, extended operational lifespan, and minimal maintenance requirements. The chosen motors operate at a relatively high nominal voltage of 48 V for improved efficiency.

To harvest solar energy, copper indium gallium selenide (CIGS) solar cells were selected. While CIGS panels have a lower efficiency (~15%) compared to alternatives such as gallium arsenide (GaAs) triple-junction (~26%) or monocrystalline silicon panels with (15%-20%), they offer advantages in other critical areas. Specifically, CIGS panels are lightweight and highly flexible, allowing better integration with the wing structure, and exhibit higher durability and weather resistance. The required area of panels required can be found using the following relationship:

$$A = \frac{2P_{total}}{Irradiance \cdot \eta_{panels}} \quad \text{Eq. 10}$$

where irradiance is measured in Wm^{-2} . With Equation 10, and using the calculated P_{total} value of 4.83 kW, a conservative sea-level irradiance value of 1000 Wm^{-2} (the value will be higher at an altitude of 55,000 ft.), and a panel efficiency of 0.15, a maximum required area of 476.23 ft^2

was determined for the solar array.

To optimize solar energy utilization in lithium-ion batteries, a Maximum Power Point Tracker (MPPT) boost converter is planned for the propulsion system. This component is similar to a typical DC-to-DC converter, but it ensures that the solar panels distribute power at maximum efficiency, thereby extending flight duration and overall energy management.

E. Propellers & Motor Casing

Variable pitch propellers were selected for both motors due to low air density at high altitudes, which requires higher pitch angles for efficient thrust. The ability to adjust the pitch during climb improves lift and provides optimal payload capacity. A low number of blades supports a lightweight design, where greater diameters generate higher thrust at lower speeds, accommodating the aircraft flight conditions.

When deciding on the shape of the propellers, five different airfoils were implemented in the design. Each airfoil has a unique size, shape, and angle of attack, in order to amplify the aerodynamic performance. At the root, the propeller experiences a lower rotational speed, in comparison to the tip of the propeller (Kramer, 2022). Because of this, the team decided to utilize thicker airfoils, longer chord lengths, and much larger angles of attack for the airfoils closest to the root. In contrast, the airfoils furthest from the root, closest to the tip, were thinner and had smaller chord lengths since this is where the propeller will encounter greater rotational speeds. Due to the varying airfoils, the blades will also have less difficulties from stalling when undergoing larger rotational speeds. See Figure 17 below for propeller and motor casing design (all dimensions in inches).

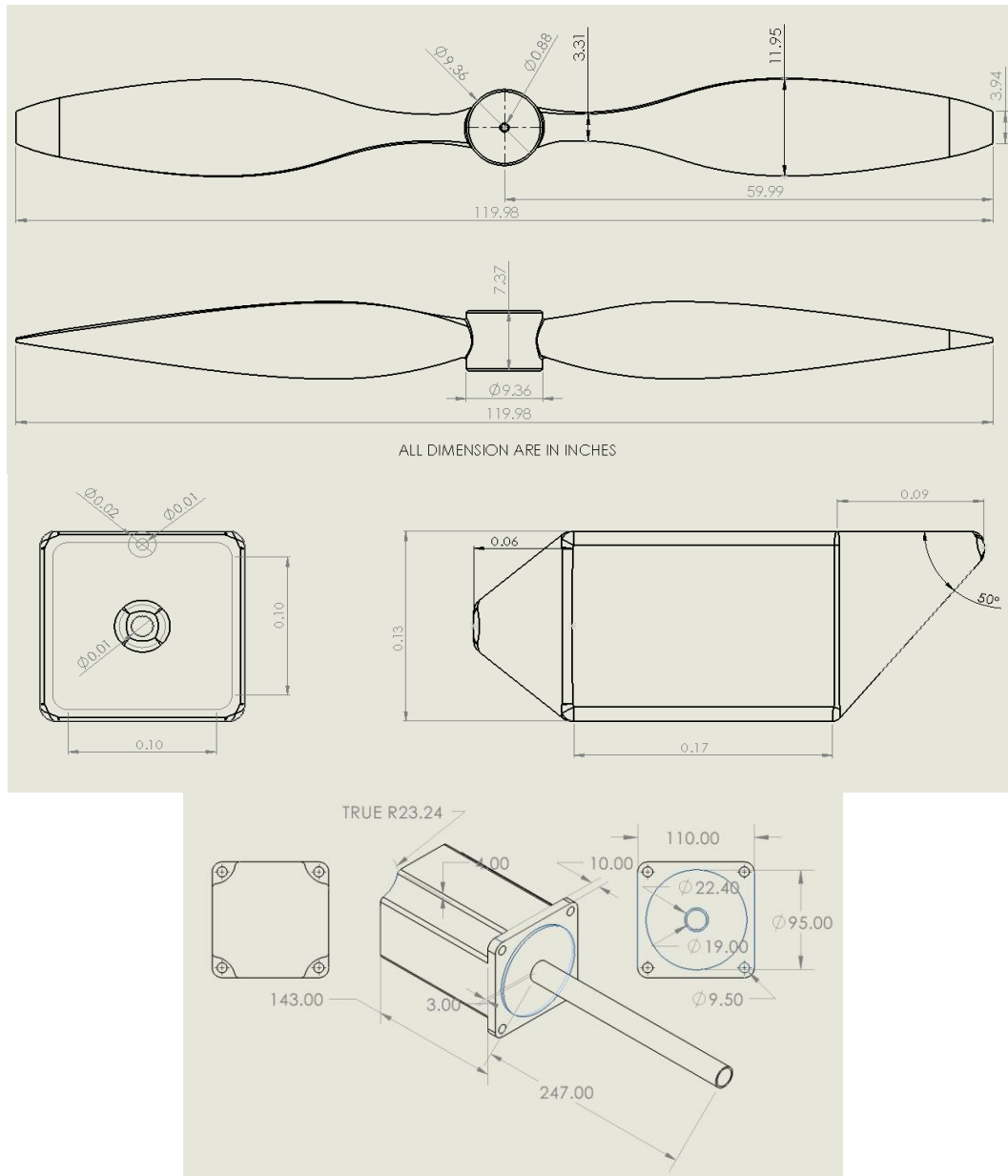


Figure 17: CAD drawing of (top) propeller, (middle) motor casing, (bottom) motor

F. Simulation

The motivation for conducting a simulation was to evaluate the aircraft power performance based on given structural design and mission parameters, and to visualize key components of the propulsion system. Simulation was initially preferred over benchtop testing due to feasibility, time constraints, and budget concerns. The primary goal of the propulsion simulation is to ensure adequate power through a 24-hour flight envelope with a consistent power output of 2740-watts at at 55,000 feet altitude.

MATLAB Simulink was utilized to run the propulsion simulation, chosen over alternative software such as Solidworks Electrical due accessibility and extensive online library of

aerospace-relevant components. Additionally, precedent projects like Solar Impulse II employed MATLAB Simulink for propulsion modeling, contributing to a broader body of literature and validated methodologies for simulating solar-powered propulsion systems. A customizable and online electrical component analysis model for hybrid and electric aircraft was selected as the simulation foundation. A solar power system was incorporated into the existing electric aircraft system.

As shown in Figure 18, the simulation integrated inputs from the mission profile (eg., altitude and flight range), aircraft parameters (eg., take off weight, wing area, lift, cruise velocity), and power components (eg., power density, capacity). These inputs produced outputs tracking battery states, current, power levels, mission progress (altitude and speed), power output, and total energy consumption.

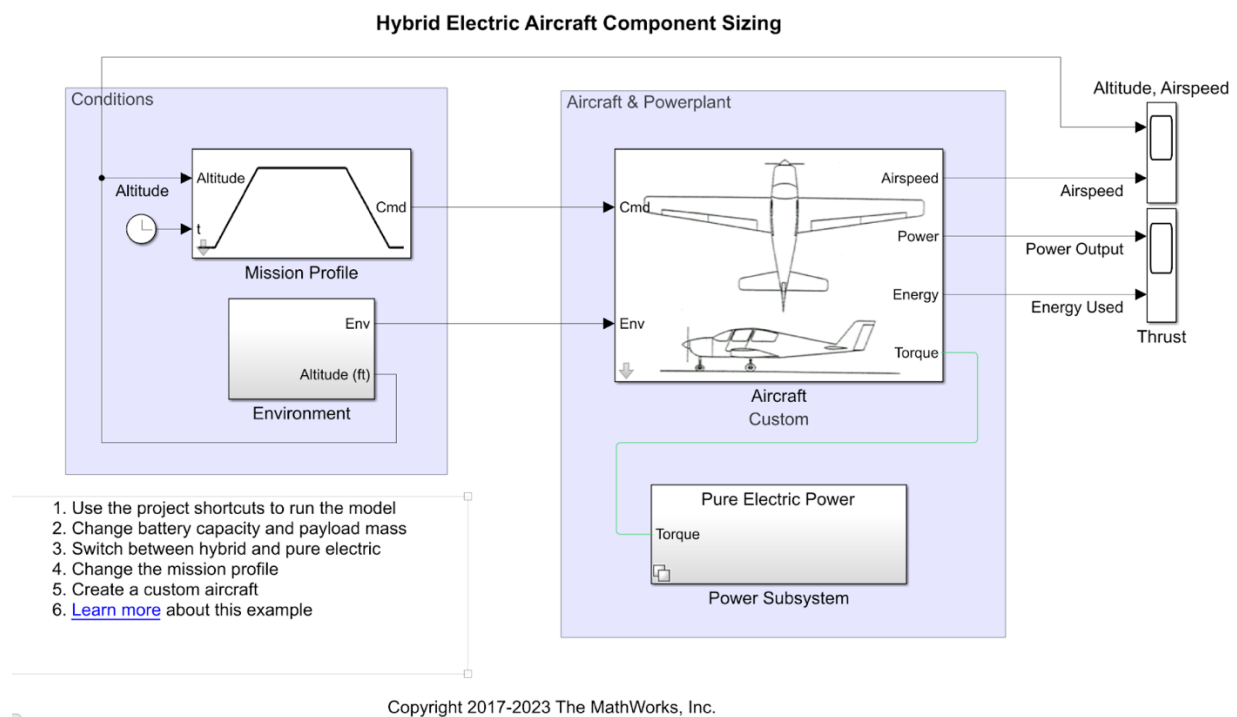


Figure 18: Electric aircraft component analysis overview on Matlab Simulink

Figure 19 portrays the electrical motor system that accounts for solar power. The model first considers irradiance, which depends on factors such as altitude, tilt of wing surface, and the height of the sun above the horizon. The power collected by the solar panels is fed into the MPPT, which is labeled as Boost Converter on the schematic. The managed current in the MPPT is then transferred to the motor, and the generated torque powers the rest of the aircraft systems to calculate the output parameters.

The propulsion simulation was not fully executed with the integration of the solar panels due to the system's complexity. However, a general schematic illustrating a power subsystem with integrated solar panels was developed, as can be seen in Figure 20. These systems were developed by using existing research and public online databases, and will

provide a greater foundation and understanding for the future developments of propulsion systems in solar powered plane design.

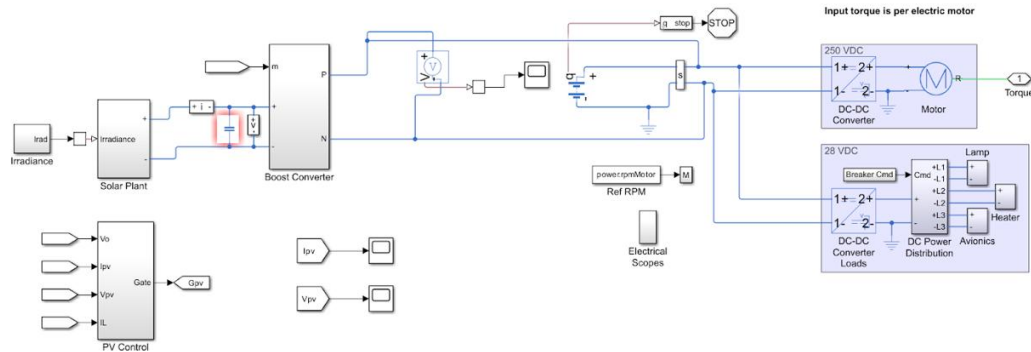


Figure 19: Electric motor schematic with solar panel input

Work remains to be done in fully integrating the solar array with the aircraft model. Factors such as code mismatch and signal conversion between the solar array subsystem and the aircraft model prevented the full simulation of a solar flight envelope within the timeframe. It is suggested that future students integrate the solar array with the full model to create a proof of concept for the theoretical power budget.

G. Component Tests

Four solar panels (500 W and 24 V each), a DC to DC converter (24-48 V), and a brushless DC motor (1500 W, 48 V) were purchased to test general solar efficiency and the aircraft's selected motor type efficiency. While the components are not identical to the conceptual components (monocrystalline silicon solar panels were purchased instead of the selected CIGS panels, and a 1.5 kW motor was used instead of a 3.5 kW one), they stand to demonstrate efficiency in panel circuit layout and electrical-mechanical power transmission. The initial test consisted of a voltage and current test to ensure that the panels provided the adequate power necessary for flight. The secondary test consisted of testing the torque of the motor connected to the solar panels to determine the mechanical energy output to find the motor efficiency.

To conduct the solar panel test, a multimeter and an ammeter were connected to find the voltage and current respectively. A separate ammeter was used because the multimeter was rated at 20 amps, significantly less than the current output needed around 33 amps. The panel tests yielded a result of 24 volts and 33 amps. In addition, the voltage step-up in the 24-48V DC-to-DC converter connected to the solar panels was measured using a multimeter, and the output was 48V, which met the system's required specification. This data was enough power to move on to the motor tests.

The motor test used a rope break test to determine load and angular velocity components to calculate the torque, which was used to find mechanical energy. The rope break test was set up as visualized by Figure 20 below. A 3D printed flywheel attached to the motor and a rope was strung around the flywheel. A load cell was connected to the top end of the rope and an accelerometer was attached to the flywheel. Weights were then added for every test and the average load and velocity were taken as data from the load cell and accelerometer respectively.

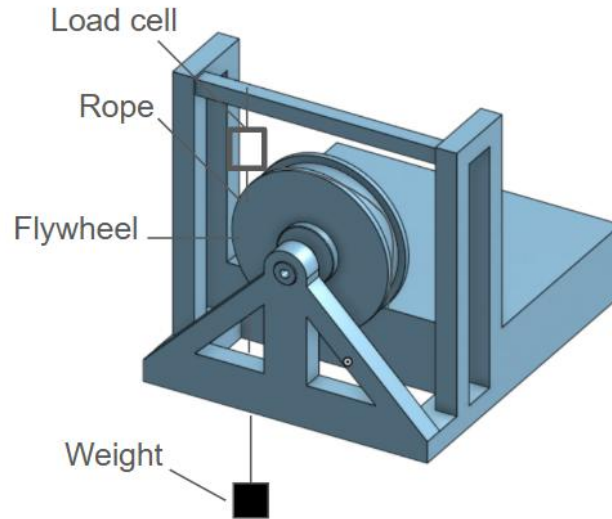


Figure 20: Rope-brake dynamometer visualization

From Equation 11, the torque of can be calculated using force on the load cell. Equation 12 finds mechanical power output from the torque and measured angular velocity using a tachometer on the flywheel axle. Equation 9 shows how to calculate the motor efficiency using a ratio between the electrical energy input into the motor and the mechanical energy output from the motor.

$$\tau = Fr \quad \text{Eq. 11}$$

$$P = \tau\omega \quad \text{Eq. 12}$$

$$\eta_{motor} = \frac{P_{in}}{P_{out}} \quad \text{Eq. 13}$$

Future steps for the propulsion systems include conducting the benchtop tests. This would aid in understanding the feasibility and efficiency of the existing aircraft propulsion design and component selection. Additional recommended tests include measuring the motor's revolutions per minute (RPM) under varying levels of irradiance. This could be tested by tilting the angle of the solar panels or covering parts of the solar panels in order to test the RPM and efficiency of the motor in varying irradiance values. It would be beneficial to predict irradiance levels at an altitude of 55,000 feet and during the aircraft's climb phase.

H. Conclusion

The SPARC aircraft propulsion and solar investigation resulted in a system consisting of approximately 476.2 square feet of CIGS solar panels, a 240.7 *kg* lithium ion battery configuration, a charge controller, an MPPT boost converter, two 3.5 *kW* brushless DC motors, and two variable-pitch propellers. Analytical proof of concept shows adequate power generation and distribution capabilities with the selected design. Component masses were fed back to the aerostructures team throughout the design iteration process, and convergence on the above values leads to reasonable confidence in design viability. Significant foundations were laid in simulation and benchtop test design in order to further verify the feasibility of calculations and aircraft design.

IX. Systems Integration: Software, Avionics, & Communications Design

Integrating avionics and software systems is essential to the operation of the SPARC aircraft. Incorporating critical components allows the aircraft to perform reliable flight control, navigation, and communication capabilities. The design utilizes a network of hardware and software components, enabling stable flight operations with common and control functionality. While systems integration is one of the project's final steps, it is pertinent to the success of every mission for future use.

The Holybro Pixhawk 6x-RT flight computer sits at the core of the avionics systems. The specific model for the onboard flight computer was chosen because of industry-backed performance and necessary redundancies within the packaged hardware. It also serves as a central processing unit for all incoming and outgoing data. More specifically, the flight computer aggregates the data from each onboard sensor and executes flight controls to maintain stability and follow the desired flight path. For redundancy, the broader avionics architecture includes a dual GPS system and backup IMUs, among other components. Redundancy is essential to operational safety and is especially important because the aircraft's extended flight capabilities require consistent system performance.

The software integration follows a three-tiered approach to achieve autonomous, long-distance, long-duration flight. The ground control software, QGroundControl, provides a user interface for mission planning and real-time monitoring of flight operations. QGroundControl is an open-source software compatible with most laptop and tablet devices, providing flexibility for launch and recovery site location. Aside from its flexibility, it was important to select a software that is able to perform all aircraft goals including calibration of the ArduPilot-powered vehicle, autonomous mission planning, flight data monitoring, and telemetry data visualization. ArduPilot software is a firmware that runs directly on the onboard flight controller. Its role within the larger avionics architecture is handling all flight control functions such as stabilization, navigation, and mission execution. The chosen communication protocol, MAVLink, standardizes data languages for communication between the ground control station and aircraft.

Regarding the communication protocol, the system utilizes multiple communication pathways to ensure connectivity across varying distances. Specific to short and medium flight, the RFD900x+, an ultra-long-range radio modem, provides the primary telemetry communication for standard operations. The advantage of having this addition is the high bandwidth of data transfer within line of sight, making landing and takeoff higher-confidence

maneuvers. The long-range global coverage communications will run through the Iridium 9603 satellite module with a dedicated low-profile Antcom antenna. Global communication coverage and command functionality in remote locations are essential for the long-range missions the aircraft will endure. In this case, conventional radio systems are not sufficient. The satellite-based system is separate from the GPS receivers, offering two-way data transfer instead of receiving one-way position signals. While the GPS receivers do not offer long-range effective communication transfer, they are important, particularly during critical flight phases like takeoff and landing. Real-time kinematic (RTK) technology utilized by the u-blox ZED F9P GPS module uses base station correction data to achieve centimeter-level accuracy.

The current design does not include a particular off-the-shelf power management system (PMS) due to the complexity of including renewable energy within the aircraft design. Therefore, the current optimal solution is a customized solution that can effectively and efficiently distribute power from the solar cells and batteries to various aircraft systems. The PMS is crucial for maintaining power across all avionics components. For a visual representation of the avionics system, see Figure 21 below.

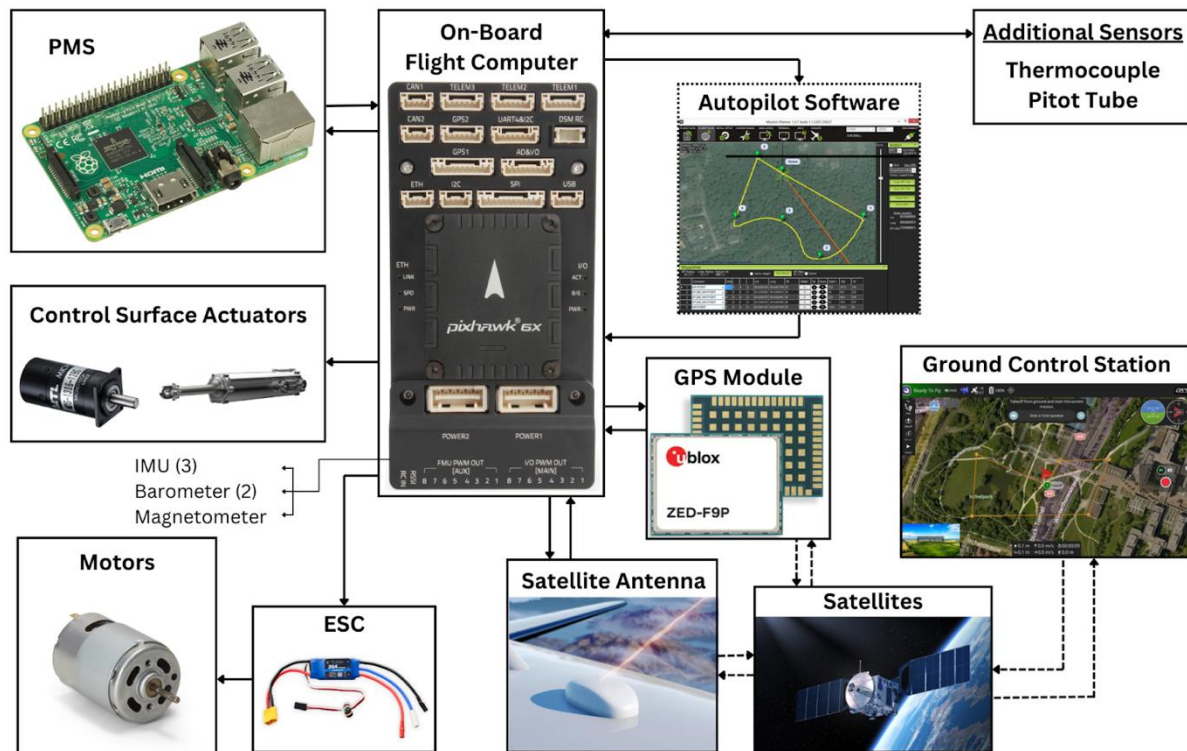


Figure 21: Aircraft Systems Component Diagram

To clearly define the avionics integration, the system is best explained using a structured flight test from takeoff to cruise. Beginning with takeoff, the ground control station communicates with the aircraft via MAVLink protocol through telemetry radio or the Iridium satellite system. The onboard flight computer processes commands and sensor data from takeoff to cruise utilizing the ArduPilot firmware. Interfacing directly with actuators (ailerons,

elevator, rudder) and the electronic speed controllers (ESCs), the flight computer continues to manage aircraft propulsion and control surfaces while following the desired flight path. Sensor inputs are then continuously monitored and processed to maintain mission parameters. This system is a robust and effective means for autonomous operations with appropriate oversight. Overall, the integration of the chosen system balances functionality with operational reliability.

X. Aircraft Performance, Stability, and Dynamics

The team relied heavily on XFLR5 for aircraft design and analysis throughout this process, and in this section gives a brief look into the design process and reports all relevant metrics to assess the current design. The current aircraft design is shown below in Figure 22, along with images of several designs along the way.

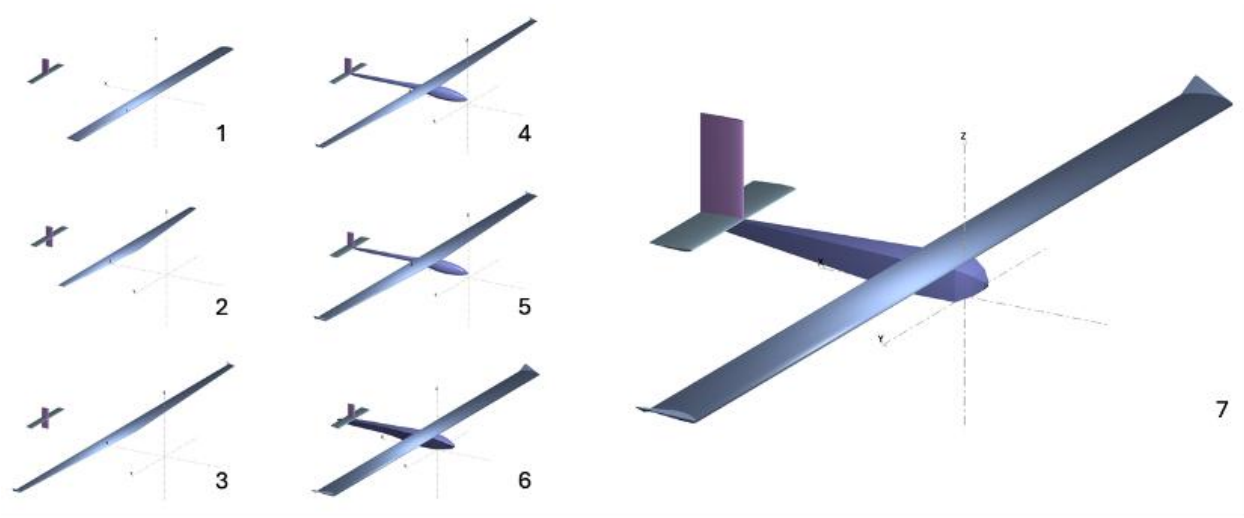


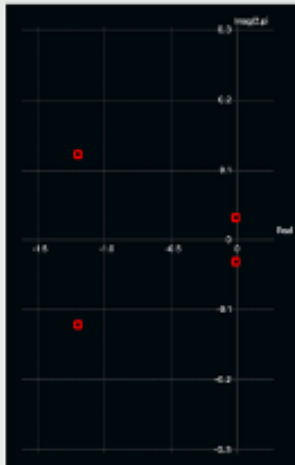
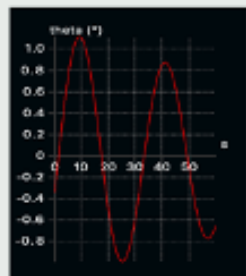
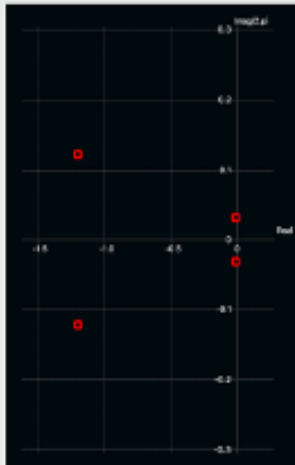
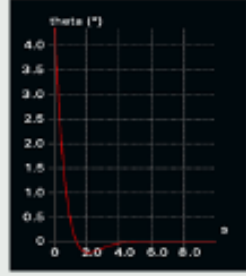
Figure 22: Final Aircraft Design with Images of Previous Designs

The first design includes a high-aspect ratio rectangular wing and conventional tail, inspired largely by the Solar Impulse 2. The next design explores a cross-tail and shifts to a trapezoidal planform, increasing the aspect ratio and aerodynamic efficiency (as measured by lift-to-drag ratio). The 3rd design expands the wingspan for higher lift, approaching the team's wingspan constraint. This design also adds winglets to the wings, reducing induced drag. The longer span and winglets largely increase the aircraft's efficiency. As wing area grows, tail volume must grow as well to maintain stability, so the fuselage was extended to push the tail back. Design 4 introduces a pod-like aerobody and reverts to the conventional tail, because it is preferred for the rear landing gear. Between designs 4 and 5, the Aerostructures team reported weights higher than budgeted, so the 5th design features and increased chord length. This sacrifices some efficiency but increases lift. Similarly, the 6th design reverts to a rectangular planform, as explained previously under the wing shape trade study. The fuselage was also changed to a triangular truss design, like that of the Solar Impulse 2. These two changes sacrifice efficiency for ease of design. The final design implements a rectangular truss fuselage,

as researched by the Structures team, and a larger horizontal and vertical stabilizer to account for the large wing area.

The current aircraft features a lift-to-drag ratio of 38.8 at its cruise altitude of 55,000 *ft*. This is more than double most airliners, which have L/D ratios of 15-20 typically. The aircraft will cruise at 73.1 *kts* (about 84 *mph*), and needs to reach 25.3 *kts* (29 *mph*) for takeoff at sea level. Negative $C_{m_{\alpha}}$ and $C_{l_{\beta}}$ values were used to verify longitudinal and lateral static stability.

After properly importing all masses into XFLR5, a final mass of 845 *lbs* was calculated. Moments of inertia are $I_{xx} = 3134 \text{ slug} - \text{ft}^2$, $I_{yy} = 1095 \text{ slug} - \text{ft}^2$, and $I_{zz} = 4133 \text{ slug} - \text{ft}^2$. These values were used to perform stability analyses. For phugoid, short period, roll, and Dutch Roll modes, root-locus plots were generated to determine frequencies and damping coefficients, as reported below in Figure 23. A mass budget can be found in Appendix G.

Mode	Constants	Root-Locus	Oscillation
Phugoid	$F_n = 0.031 \text{ Hz}$ $F_d = 0.031 \text{ Hz}$ $\zeta = 0.04$		
Short Period	$F_n = 0.225 \text{ Hz}$ $F_d = 0.121 \text{ Hz}$ $\zeta = 0.84$		

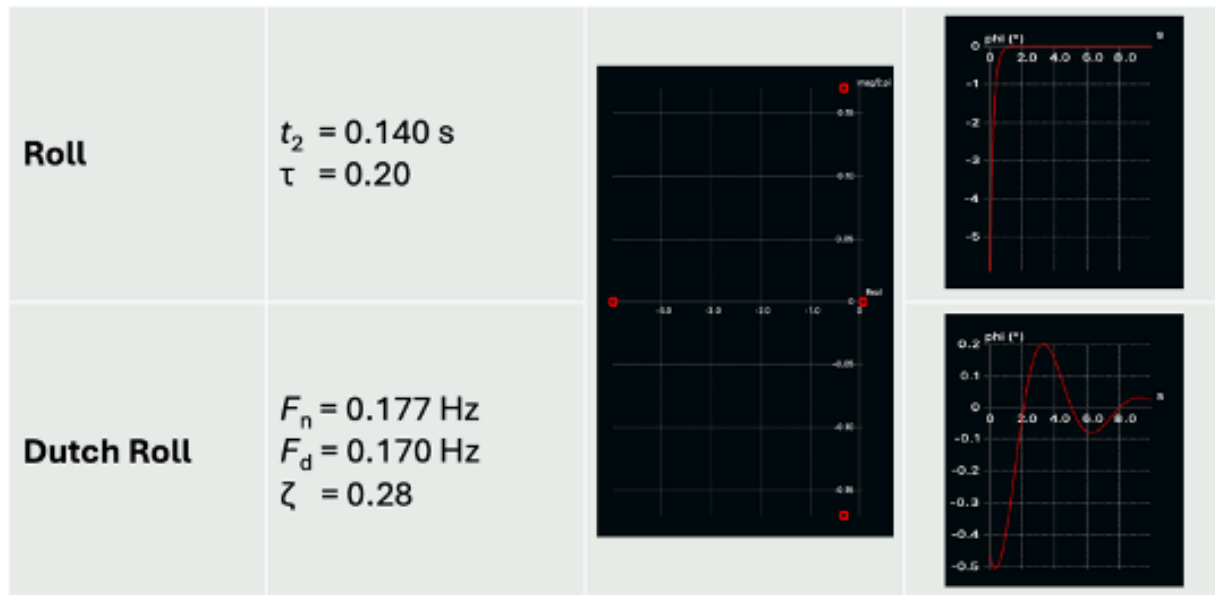


Figure 23: Dynamic Stability Values and Plots in Four Natural Modes

The aircraft is controlled by ailerons, elevators, and a rudder. Control surface spans and chords were set as percentages of the wing, horizontal stabilizer, and vertical stabilizer. A MATLAB script was written to evaluate the lift produced by each surface at its maximum deflection angle. Using these forces along with aircraft geometry and mass properties, rotational moments were calculated and then kinematically simulated to find typical rotation rates. Figure 24 below summarizes this data.

Control Surface	Span (ft) [% Of Wing/Stabilizer span]	Chord (ft) [% Of Wing/Stabilizer Chord]	Typical Rotation Rate (deg/s)
Aileron	12 [30]	1 [22]	35
Elevator	14 [90]	0.52 [20]	20
Rudder	7.86 [100]	1.5 [40]	5

Figure 24: Control Surface Parameters and Roll, Pitch, and Yaw Rates

XI. Suggestions for Future Work

At the conclusion of this project, the SPARC team would like to recommend important next steps for any continuation of this work. There are aspects of this report that the team would like to have completed, but did not do so by the conclusion of the academic year, and there are further tests and simulations that could enhance the current aircraft design.

Further steps could be taken to reduce the mass of the aircraft through detailed FEA analysis. Now that a full aircraft CAD assembly has been created, static simulations are to be performed including accurate mates, fixtures, and loads that would exist in flight. A visualization of safety factor or stress on all structural members would illuminate sections where material should be reduced or added to optimize the aircraft's strength per weight.

Further work would also be beneficial in control surface analysis. At the current stage, the team has simulated roll, pitch, and yaw to calculate baseline rotation rates in all 3 axes to verify functionality of the designed flight surfaces. However, these calculations are an oversimplification, accounting for exactly one control surface in each axis despite the reality that these are paired, such as yaw and roll both being impacted by the rudder and ailerons. To better understand the effectiveness of these surfaces, a CFD simulation should be run with various control surface deflections for more accurate results.

The whole aircraft should also be simulated in CFD to confirm the accuracy of reported lift and drag coefficients. The solver in XFLR5 uses a simplified panel method and has inaccuracies in the viscous simulation. It also fails to account for body-wing interactions. Therefore, a proper mesh of the aircraft should be generated and simulated in all phases of the flight envelope.

XII. Conclusion

The mission of the SPARC project was to demonstrate the feasibility of designing a highly modular, autonomous, solar-powered aircraft capable of supporting a diverse range of surveillance and exploration missions. Through innovative design using computer-aided software, extensive power, stability, and structural strength simulations, and interdisciplinary collaboration, the sub-teams addressed critical challenges associated with developing a sophisticated solar-powered aircraft capable of meeting the team's mission objectives. Additionally, the project provided invaluable experiential learning opportunities, equipping undergraduate aerospace engineers with the skills necessary to lead the next generation of sustainable aircraft development. The SPARC team advanced the practical application of solar energy in present-day aircraft and laid the foundation for continued research and development in support of the SPARC mission, helping to shape the future of sustainable, long-endurance flight.

XIII. Resources

Abbott, R. (2019). 22.16.2. Main wing box. *Abbott Aerospace Canada Ltd.*
<https://www.abbottaerospace.com/aa-sb-001/22-aircraft-specific-design-features-and-design-methods/22-16-57-wings/22-16-2-main-wing-box/>

Anderson, J. D. (1999). *Aircraft performance and design*. WCB/McGraw-Hill.

Aviation Week Network. (2025). *Aircraft overview: Gulfstream G650 / G650ER*. Aviation Week Network. <https://aviationweek.com/business-aviation/aircraft-overview/aircraft-overview-gulfstream-g650-g650er>

Blaesser, N. J., & Frederick, Z. J. (2020). *Tail sizing considerations for wingtip propulsor driven aircraft applied to the Parallel Electric-Gas Architecture with Synergistic Utilization Scheme (PEGASUS) Concept* (NASA Technical Report No. 20200010339). NASA Langley Research Center. <https://ntrs.nasa.gov/api/citations/20200010339/downloads/20200010339.pdf>

Craig, D. (2007, February 28). *Math methods: Wingtip vortices*. Retrieved from 070228_wingtip.pdf

Diehl, W. S. (1923). *Notes on the design of ailerons* (NACA Technical Note No. 144). National Advisory Committee for Aeronautics. <https://ntrs.nasa.gov/citations/19930081054>

Dong, H., Liu, S. C., Geng, X., Cui, Y. D., & Khoo, B. C. (2018). Letter: A note on flow characterization of the FX63-137 airfoil at low Reynolds number using oil-film interferometry technique. *Physics of Fluids*, 30(10), 101701. <https://doi.org/10.1063/1.5052233>

FX 63-137 airfoil (fx63137-il). (n.d.). *Airfoil Tools*. Retrieved April 9, 2025, from <http://airfoiltools.com/airfoil/details?airfoil=fx63137-il>

Glider performance efficiency. (n.d.). *ScienceDirect*. Retrieved April 23, 2025, from <https://www.sciencedirect.com/science/article/pii/S0029801820305758>

García-Ortiz, J. H., Domínguez-Vázquez, A., Serrano-Aguilera, J. J., Parras, L., & del Pino, C. (2019). A complementary numerical and experimental study of the influence of Reynolds number on theoretical models for wingtip vortices. *Computers & Fluids*, 180, 176–189. <https://doi.org/10.1016/j.compfluid.2018.12.009>

Giuni, M. (2013). *Formation and early development of wingtip vortices* [Doctoral dissertation, University of Glasgow]. Glasgow Theses Service. <http://theses.gla.ac.uk/3871/>

Kramer, T. (2022). *Why are airplane propeller blades twisted?* Airplane Academy. <https://airplaneacademy.com/why-are-airplane-propeller-blades-twisted/>

NASA Glenn Research Center. (n.d.). Rudder. NASA. Retrieved April 16, 2025, from <https://www.grc.nasa.gov/www/k-12/VirtualAero/BottleRocket/airplane/rud.html>

Reddy, S. R., Sobieczky, H., Abdoli, A., & Dulikravich, G. S. (n.d.). Winglets – Multiobjective optimization of aerodynamic shapes. *11th World Congress on Computational Mechanics (WCCM XI), 5th European Conference on Computational Mechanics (ECCM V), 6th European Conference on Computational Fluid Dynamics (ECFD VI)*. Retrieved from H206.pdf

Scholz, D. (2021). Empennage sizing with the tail volume complemented with a method for dorsal fin layout. *INCAS Bulletin*, 13(3), 149–164. <https://doi.org/10.13111/2066-8201.2021.13.3.13>

Traub, L. W. (2024). Prediction of the Oswald efficiency factor for cambered and swept wings. *Journal of Aircraft*, 61(1), 317–322. <https://doi.org/10.2514/1.C037444>

University of Virginia Department of Mechanical and Aerospace Engineering. (2025). *MAE 3820 introductory laboratory activity: Particle image velocimetry (PIV)*. Internal course material. Retrieved from MAE3820_PIV_Activity.docx

University of Virginia Department of Mechanical and Aerospace Engineering. (2025). *PIV lab activity: Sample solutions*. Internal course material. Retrieved from PIV Activity Sample Solutions.docx

XIV. Appendices

Appendix A Functional Requirements, Operational Requirements, and Mission Constraints

Table 1A: Functional requirements for the SPARC aircraft

ID	Function	Quantitative Performance Requirement	Verification Method
F-1	Performance	Minimum TO Climb Rate ~ 300ft/min	Benchtop Solar Test
F-2	Performance	L/D > 25	XFLR5 Software Analysis
F-3	Energy Collection & Storage	Energy necessary to sustain flight during 12hr of darkness with minimum altitude lost	Sub-scale & Benchtop tests
F-4	Autonomous Control & Navigation	Navigate mission flight path with < 100m deviation	Avionics Testing & Performance Analysis
F-5	Data Processing	Process and transmit mission data in real time with < 1s latency	Benchtop Electronics/Avionics Test

Table 2A: Operational requirements for the SPARC aircraft

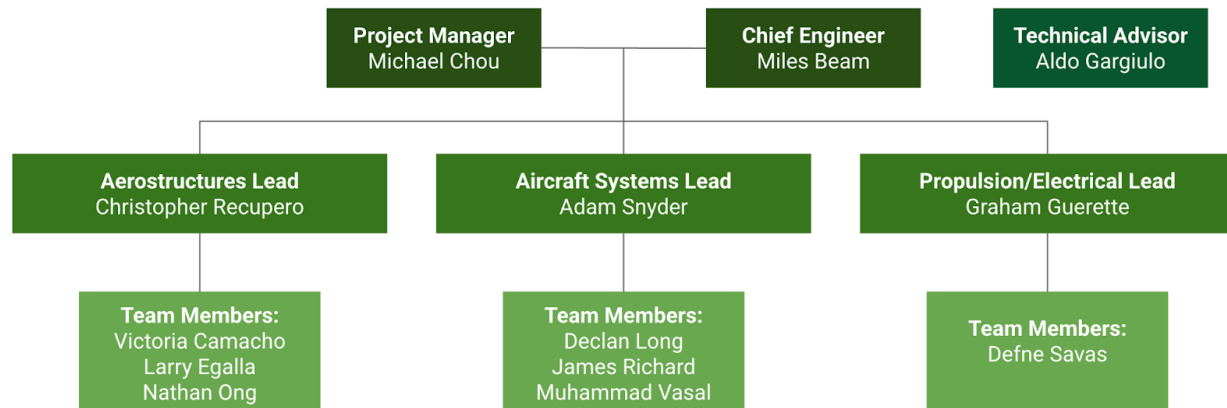
ID	Operation	Quantitative Performance Requirement	Verification Method
O-1	Atmosphere	Withstand temperatures -60 to 40°C and radiation at cruising altitudes	Flight Test
O-2	Altitude	Continuous communication up to 55,000 ft altitude	Flight Test
O-3	Mission Duration	Continuous operation for 60 days	Demonstration

O-4	Sunlight	Operate continuously with minimum 12 hours of sunlight per day	Demonstration
-----	----------	--	---------------

Table 3A: Mission constraints for the SPARC aircraft

ID	Constraint	Description
C-1	Size	100 ft. maximum wingspan due to hangar limitations
C-2	Regulations	Limited location and altitude without certain certifications or licenses
C-3	Cost	Commercially viable cost of \$2 million – Intended for governments & scientific orgs.
C-4	Technology Availability	Limited in power and efficiency to solar panel and battery technologies, among others

Appendix B Team Structure Graphic



The aerostructures team focused on the physical design of the aircraft, including airfoil selection and producing a full computer-aided design model of the aircraft, utilizing industry-standard software tools to aid in the design process. The aerostructures team also attempted to run computational fluid dynamics tests of the wing design. However, most of the team’s effort was spent contributing to physical experiments using the PIV water tunnel and the wind tunnel for winglet and airfoil tests

The power/electrical team focused on the electronic system of the aircraft, which included selecting the optimal electrical components, such as solar panels and motors. The power team also ran simulations on the Electrical Component Analysis using a “Hybrid and

Electric Aircraft Matlab program,” which runs simulations and provides a flight envelope for an electrical aircraft. It was modified to provide data for this project’s solar-powered aircraft.

The systems team focused on the integration of the different components of the aircraft, including the design of the landing gear and fuselage of the aircraft. The systems team also ran finite element analysis for identifying load-bearing components of the aircraft, and analyzed aircraft static and dynamic stability in the preliminary stages of design. Finally, the team assisted other sub-teams in component location, organizing the weight balance of the aircraft, and running trade studies to make wing design choices.

The 3 subteams worked together to design the solar-powered aircraft, and the design progress of the entire team is specified in this report.

Appendix C **Team Budget, Proposed & Current Spendings**

Table C1: Total Team Budget

Funding	Estimated Value (USD)
Aerospace Capstone Funding	12 x \$200
Total	2400

Table C2: Original Planned Budget Distribution

Teams	Material/Details	Cost Distribution
Power/Electrical	Solar Panels, Converter, Motor, Propeller	40%
Structural/Aerodynamics	CFRP Samples, 3D Filament for Test Models	35%
Systems	Actuators, Communications Equipment, 3D Filament for Testing	23%
Admin	Other Project Supporting Costs	2%
Total		100%

Table C3: Current Spendings

Item	Details	Cost
Budget	\$200 x 12 Team Members	2400

Brushless DC Motor	ATO 2 hp (1.5 kW) Brushless DC Motor, 36V/48V, 4.78 Nm	- 432.36
DC Converter	Clleena Waterproof DC/DC 24V 36V to 48V Boost Converter 40A 1920W Step Up Voltage Regulator Module Car Power Supply Voltage Transformer (Input 20V-42V)	- 169.99
Solar Panels	2000 Watt Solar Panel Kit, with car Inverter and 40A Charge Controller 4pcs 500 Watt Flexible Monocrystalline Solar Panel for 12-48V Battery Charging Car Battery Camper RV Yacht Boat	- 869.99
Admin	Miscellaneous Materials for Capstone	-64
Total Left Over		863.66

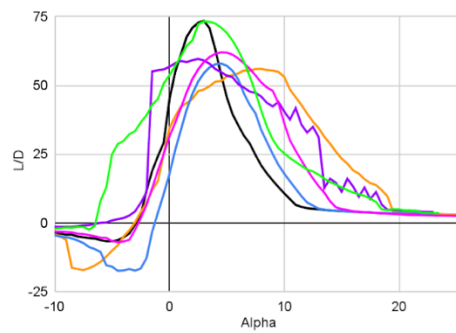
Table C4: Total Proposed Aircraft Budget (Raw Parts Only)

Component	Material/ Details	Total Estimated Cost (USD)
Wing Structure	CFRP, Mylar	1700 – 1800
Empennage Structure	CFRP	250 – 300
Fuselage Structure	CFRP, Mylar	550 – 600
Solar Panels	CIGS Flexible Polymer Substrate	15000 – 16000
Batteries	Custom Power Li-ion Battery Pack	3000 – 6000
Engines/Propellers	ATO 4 hp BLDC Motor, Airmaster Variable Pitch	36000 – 60000
Onboard Computer	Holybro Pixhawk 6x-rt, ZED-F9P GPS	500 – 900
Communication Antennae	Iridium 9603 Module & Antenna, GNSS Antenna	1700 – 1900
Flight Control Actuators	Pistons, Control Surfaces	1500 – 4500
Payload	Sensors & Cameras	10000 – 20000
Miscellaneous	Takeoff/Landing Vehicle, Other Unplanned Components	15000 – 30000
Total		85200 – 142000

Appendix D Airfoil comparison

- **A18**
 - Narrow range of high performance, steep decline in L/D past peak
- **NACA 4415**
 - Common sailplane airfoil
- **RG15**
 - Low drag airfoil used in low Re applications (like windmills)
- **SI223**
 - Designed for high lift at low Re by aerodynamics professor Michael Selig at UIUC
- **SD7037**
 - Also designed by Selig, used in low Re, UAV applications
- **FX 63-137**
 - Used for high altitude slow velocities

XFLR5 Data

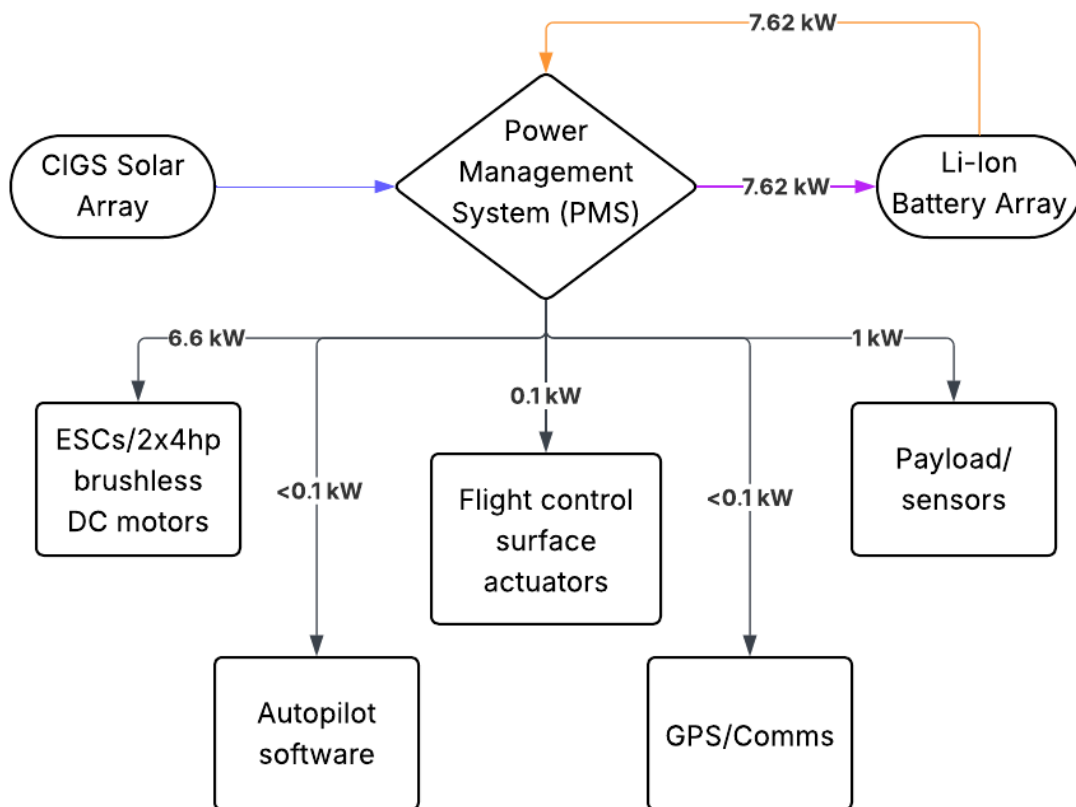


Appendix E Risk Management Matrices

Risk Name	Risk Type	Likelihood	Consequence	Priority Score
Battery Thermal Runaway or Explosion	Safety	1	5	12
Aircraft Collision with Terrain, Structures, or Individuals	Safety	1	5	12
Environmental Contamination (ice & dust)	Safety	4	2	13
Solar Energy Deficiency	Technical	2	5	17
Lost connection to flight computer	Technical	2	4	14
Propulsion System Failure	Technical	1	3	5
Perceived High Cost by Customers	Cost	2	5	17

Excessive Maintenance or Repair Costs	Cost	2	3	11
Inadequate Project Funding	Cost	5	1	7
Delays in Part Delivery or Supply Chain Disruptions	Schedule	4	4	18
Fabrication and Assembly Schedule Delays	Schedule	4	3	18
Team Resource Shortages (Illness, Absence, etc.)	Schedule	5	2	16

Appendix F Power Budgets



— Climb conditions

— Daytime cruise operation

— Nighttime cruise operation

— Cruise (day & night)

Appendix G Mass Budgets

Category	Component	Weight	Dimensions	CG.x (ft)	CG.y (ft)	CG.z (ft)	Notes
Propulsion	Battery Weight	213.6 (lbm)	about 4 ft*3?				
	Battery with Housing (total)	220					
	Motor (1)	12.12					
	Motor (2)	12.12					
	Prop (1)	20					
	Prop (2)	20					
	Solar Panels	45		same as wing	0.000	same as wing	
		329.24					
Electronics	GPS 1: u-blox ZED-F9P	0.047	17.0 x 22.0 x 2.4 (mm)				
	GPS 2: M9N	0.071	76.3 (mm, h.); 66.5 (mm, dia.)				
	Pixhawk 6X-RT (Onboard Flight Computer)	0.163	52.4 x 103.4 x 16.7 (mm)				
	Antenna: TW3972 Triple Band + GNSS Antenna	0.408	66.5 mm (dia.) x 21 mm (h.)				
	Radio 1: RFD 900x-US Modem	0.032	30 x 57 x 12.8 (mm)				
	Radio 2: Iridium Low Profile Antcom Antenna	0.322	88.9 (mm, dia.); 14.81 (mm, h.)				
	ESCs 1: Currawong Velocity ESC	0.165	80 x 45 x 13.5 (mm)				
	ESCs 2: Currawong Velocity ESC	0.165	80 x 45 x 13.5 (mm)				
	Airspeed sensor: Holybro Digital Airspeed Sensor	0.007	17.4 x 12.4 x 7.2 (mm)				
	Actuator - Ail, L	0.500					
	Actuator - Ail, R	0.500					
	Actuator - Elev, L	0.500					
	Actuator - Elev, R	0.500					
	Actuator - Rudder	0.500					
	Subtotal:	3.8799					
				160.98			
Payload	Payload	50.0000					
		all in lb below					
Structures	Main Wing (incl. ailerons)	321.96	b=80ft (83.5 w winglet), c=4.5ft	2.272	0.000	3.324	cg.y is 21.2626 for each wing
	Horizontal Tail (incl. elevators)	21.59	b=12ft, c=2ft	19.738	0.000	3.152	
	Vertical Tail (incl. rudder)	49.50	b=3ft, c=1.5ft	19.454	0.000	4.500	
	Fuselage Truss only (32.83 lb)		21.06 x 2.6tail x 3ftwide	9.196	-0.003	1.552	front box is 2.6tail x 3wide and
	Fuselage Truss + Nose + Tail	35.79		8.799	-0.003	1.548	
	Motor Housing/Nacelle (1)	2.00					
	Motor Housing/Nacelle (2)	2.00					
	Main Landing Gear	12.37					
	Rear Landing Gear	5.00					
	Wing Landing Gear (L)	6.23					
	Wing Landing Gear (R)	6.23					
		462.67					
	NET WEIGHT (lb):	845.79					

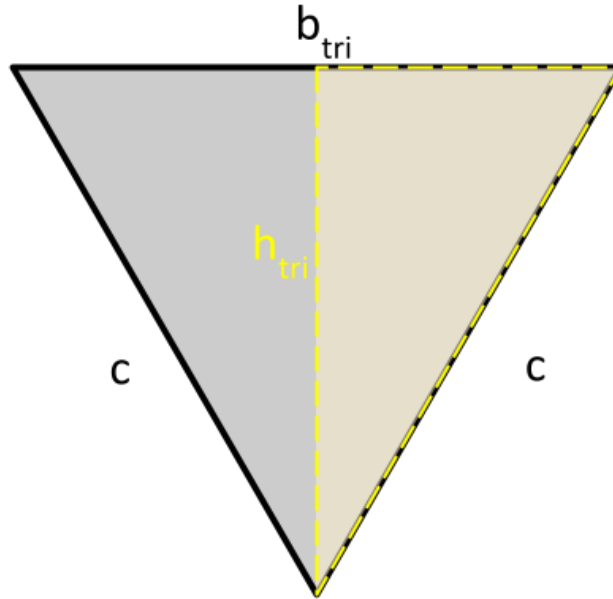
Appendix H Relevant Calculations

Fuselage Cross Section Study —

The moment of inertia of a triangle about its centroid is given by: $I_x = \frac{bh^3}{36}$

The moment of inertia of a triangle about its centroid is given by: $I_x = \frac{bh^3}{12}$

Where b is the length of the base of the shape and h is the height.



The perimeter (P) of a triangle, assuming isosceles, is given by $P_{tri} = b_{tri} + 2c$. According to the Pythagorean theorem, $a^2 + b^2 = c^2$, where a and b are two sides and c is the hypotenuse.

$$\left(\frac{b}{2}\right)^2 + h_{tri}^2 = c^2$$

$$c = \sqrt{\frac{b_{tri}^2}{4} + h_{tri}^2}$$

$$P_{tri} = b_{tri} + 2\sqrt{\frac{b_{tri}^2}{4} + h_{tri}^2}$$

The perimeter (P) of a rectangle, is given by $P_{rect} = 2(b_{rect} + h_{rect})$

To standardize the comparison, = set $b_{tri} = b_{rect} = b$. Assume an equilateral triangle and a square rectangle. This means $h_{rect} = b$ and $b = c$, meaning

$$h_{tri} = \sqrt{b^2 - \frac{b^2}{4}} = \sqrt{\frac{3}{4}b^2} = b\frac{\sqrt{3}}{2}$$

$$I_{tri} = \frac{bh^3}{36} = \frac{b\left(b\frac{\sqrt{3}}{2}\right)^3}{36} = \frac{b^4 3^{\left(\frac{3}{2}\right)}}{36 \cdot 8} = \frac{\sqrt{27}}{288} b^4$$

For a rectangle (square),

$$I_{rect} = \frac{bh^3}{12} = \frac{1}{12} b^4$$

Normalizing perimeter,

$$P_{tri} = b + 2\sqrt{\frac{b^2}{4} + h^2} = b + 2\sqrt{\frac{b^2}{4} + \left(b\frac{\sqrt{3}}{2}\right)^2} = b + 2\sqrt{\frac{b^2}{4} + b^2\left(\frac{3}{4}\right)} = b + 2b = 3b$$

$$P_{rect} = 4b$$

Set $R = \frac{I}{P}$ where a larger R indicates a larger moment of inertia relative to volume, which is more favorable.

$$R_{tri} = \frac{\left(\frac{\sqrt{27}}{288} b^4\right)}{3b} = \frac{(\sqrt{27})}{864} b^3 = 0.00601406530406 \cdot b^3$$

$$R_{rect} = \frac{\left(\frac{1}{12} b^4\right)}{4b} = \frac{1}{48} b^3 = 0.020833333333333b^3$$

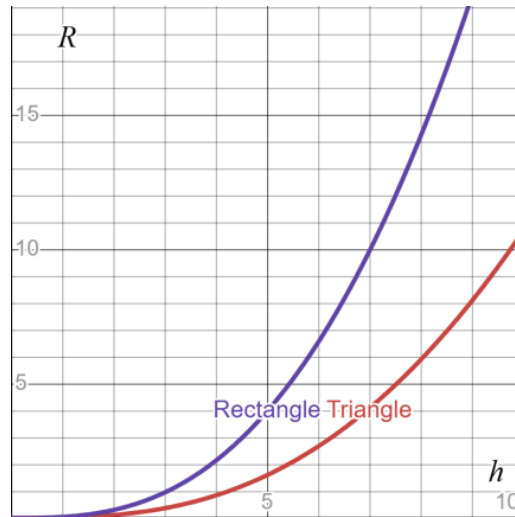
Thus, for all values of b , $R_{rect} > R_{tri}$

Assuming the shapes are *not* symmetric, such that the triangle is returned to its isosceles (but not necessarily equilateral) shape and the square rectangle to its general rectangle shape,

$$R_{tri} = \frac{\left(\frac{bh^3}{36}\right)}{b + 2\sqrt{\frac{b^2}{4} + h^2}} = \frac{bh^3}{36\left(b + 2\sqrt{\frac{b^2}{4} + h^2}\right)}$$

$$R_{rect} = \frac{\left(\frac{bh^3}{12}\right)}{2(b+h)} = \frac{bh^3}{24(b+h)}$$

Since b appears to have the same order in both R terms, it can be ignored. Graphing R as a function of h gives us Fig. 13



The trend of the graph indicates that for all values of h , $R_{rect} > R_{tri}$. Mathematical proof is shown below

Critical condition: $R_{tri} = R_{rect}$

$$\begin{aligned} \frac{bh^3}{36\left(b + 2\sqrt{\frac{b^2}{4} + h^2}\right)} &= \frac{bh^3}{24(b+h)} \\ 3\left(b + 2\sqrt{\frac{b^2}{4} + h^2}\right) &= 2(b+h) \\ 3b + 6\sqrt{\frac{b^2}{4} + h^2} &= 2b + 2h \\ b + 6\sqrt{\frac{b^2}{4} + h^2} &= 2h \\ b &= 2h - 6\sqrt{\frac{b^2}{4} + h^2} \end{aligned}$$

For R_{tri} to surpass R_{rect} , $b = 2h - 6\sqrt{\frac{b^2}{4} + h^2}$

This is impossible, because $2h - 6\sqrt{\frac{b^2}{4} + h^2}$ does not result in a positive number for all real values of b and h .

$\frac{b^2}{4} + h^2 \approx h^2$ (this is a valid assumption because $h^2 < \frac{b^2}{4} + h^2$)

$$b \approx 2h - 6\sqrt{h^2}$$

$$b \approx 2h - 6h$$

$b \approx -4h$, which is impossible

Although a triangle requires less perimeter (and therefore less mass) for the same height, the moment of inertia to perimeter ratio is lower than a rectangle, which means less material in a rectangular arrangement is used to arrive at the same strength, which is more applicable for this case.

Appendix I Airfoil Wind Tunnel Test

Wortmann FX 63-137 Airfoil at ~500,000 Re with forces averaged over 5 seconds

Angle	Wind speed (ft/s, 79mph)	Air Density (slug/ft ³)	Wing Area (ft ²)	Force (norma, lbf)	Force (axial, lbf)	Pitching moment	lift force (lbf)	drag force (lbf)	cd	cl
-10	115.8670	0.0024	0.4238	-0.7958	0.6290	8.9458	0.6745	0.7577	0.1120	0.0997
-9	115.8670	0.0024	0.4238	-0.5214	0.6290	8.9599	0.4165	0.7029	0.1039	0.0616
-8	115.8670	0.0024	0.4238	-0.1222	0.2894	9.0462	0.0808	0.3036	0.0449	0.0119
-7	115.8670	0.0024	0.4238	0.2335	0.3024	7.9645	0.2686	0.2717	0.0402	0.0397
-6	115.8670	0.0024	0.4238	0.6507	0.3257	6.1743	0.6812	0.2559	0.0378	0.1007
-5	115.8670	0.0024	0.4238	1.0497	0.3283	4.8149	1.0743	0.2355	0.0348	0.1589
-4	115.8670	0.0024	0.4238	1.5148	0.3923	2.9980	1.5385	0.2857	0.0423	0.2275
-3	115.8670	0.0024	0.4238	1.9055	0.3378	1.3681	1.9205	0.2376	0.0351	0.2840
-2	115.8670	0.0024	0.4238	2.2600	0.3228	-0.1206	2.2699	0.2437	0.0360	0.3357
-1	115.8670	0.0024	0.4238	2.9722	0.3524	-2.7019	2.9779	0.3005	0.0444	0.4404

0	115.8670	0.0024	0.4238	3.1377	0.3516	-3.5039	3.1377	0.3516	0.0520	0.4640
1	115.8670	0.0024	0.4238	3.8545	0.3152	-5.9326	3.8484	0.3824	0.0566	0.5691
2	115.8670	0.0024	0.4238	4.3331	0.2863	-7.7277	4.3204	0.4373	0.0647	0.6389
3	115.8670	0.0024	0.4238	4.9973	0.2293	-9.9955	4.9784	0.4905	0.0725	0.7362
4	115.8670	0.0024	0.4238	5.3457	0.0503	-11.5294	5.3291	0.4231	0.0626	0.7881
5	115.8670	0.0024	0.4238	5.8644	0.1396	-13.3096	5.8299	0.6502	0.0962	0.8622
6	115.8670	0.0024	0.4238	6.3397	0.0785	-15.0398	6.2968	0.7408	0.1095	0.9312
7	115.8670	0.0024	0.4238	6.5004	0.0233	-15.9218	6.4492	0.8153	0.1206	0.9537
8	115.8670	0.0024	0.4238	6.6986	0.0284	-16.7932	6.6374	0.9042	0.1337	0.9816
9	115.8670	0.0024	0.4238	6.9819	0.0966	-18.0475	6.9110	0.9968	0.1474	1.0220
10	115.8670	0.0024	0.4238	7.2488	0.1559	-19.1357	7.1657	1.1052	0.1634	1.0597
11	115.8670	0.0024	0.4238	7.2665	0.2215	-19.5408	7.1752	1.1691	0.1729	1.0611
12	115.8670	0.0024	0.4238	7.5427	0.3517	-20.6726	7.4510	1.2242	0.1810	1.1019
13	115.8670	0.0024	0.4238	7.5966	0.4715	-21.1393	7.5079	1.2495	0.1848	1.1103
14	115.8670	0.0024	0.4238	7.7000	0.5473	-21.7247	7.6037	1.3318	0.1969	1.1245
15	115.8670	0.0024	0.4238	7.7602	0.6112	-22.2304	7.6539	1.4181	0.2097	1.1319
16	115.8670	0.0024	0.4238	7.7361	0.6663	-22.3933	7.6201	1.4919	0.2206	1.1269
17	115.8670	0.0024	0.4238	7.9318	0.7522	-23.1756	7.8052	1.5997	0.2366	1.1543
18	115.8670	0.0024	0.4238	8.1324	0.8634	-24.0735	8.0012	1.6919	0.2502	1.1832
19	115.8670	0.0024	0.4238	8.1622	0.9229	-24.3873	8.0180	1.7847	0.2639	1.1857
20	115.8670	0.0024	0.4238	8.2558	1.0386	-24.9913	8.1132	1.8477	0.2732	1.1998
21	115.8670	0.0024	0.4238	8.2727	1.1182	-25.3405	8.1239	1.9208	0.2841	1.2014

22	115.8670	0.0024	0.4238	8.6103	1.2431	-26.5026	8.4490	2.0729	0.3065	1.2495
23	115.8670	0.0024	0.4238	8.8387	1.3464	-27.3657	8.6621	2.2142	0.3274	1.2810
24	115.8670	0.0024	0.4238	8.6974	1.3723	-26.8602	8.5036	2.2838	0.3377	1.2575
25	115.8670	0.0024	0.4238	8.9038	1.3453	-27.4215	8.6381	2.5437	0.3762	1.2774

Appendix J Winglet Design Study

Selection of three wingtip designs:

- Baseline wing without winglet
- Blended winglet with 30 degree upward slope
- Blended winglet with 30 degree downward slope
- Back curved winglet with 30 degree upward slope
- Double-facing back curved winglet (30 degree upward & downward slope)

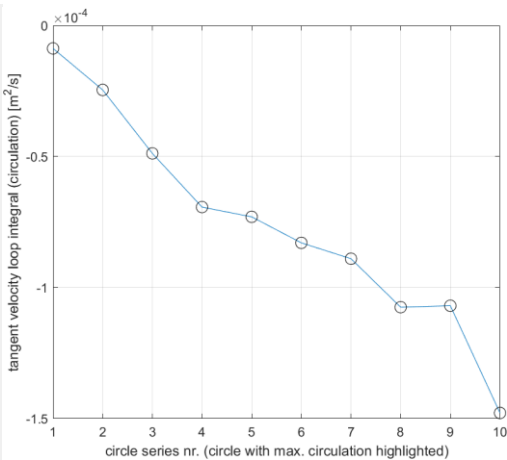
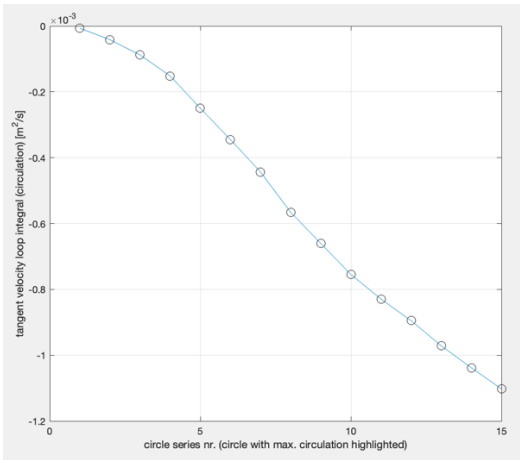
Analyzation Criteria:

Parameter	Measurement Approach	Ideal Outcome
Circulation (Γ)	Line integral of velocity field	Lower values indicate weaker vortices
Peak Vorticity (ω)	Vorticity field analysis	Lower vorticity values
Vortex Core Radius (r_c)	Core radius estimation from velocity gradient	Larger core suggests weaker vortex
Vortex Decay Rate	Strength comparison at different downstream positions	Faster decay indicates reduced wake turbulence
Downwash Strength	Vertical velocity component analysis	Lower downwash indicates reduced induced drag

Circulation (Γ)

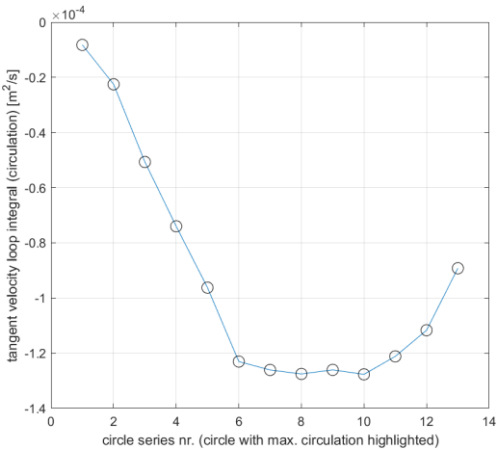
One of the primary metrics used to evaluate wingtip vortices is circulation, which quantifies the rotational strength of the vortex in units of m^2/s . Circulation is directly linked to induced drag—a higher circulation value generally corresponds to a stronger, more energetic

vortex and greater aerodynamic losses. Therefore, minimizing circulation is a key objective in optimizing winglet performance.

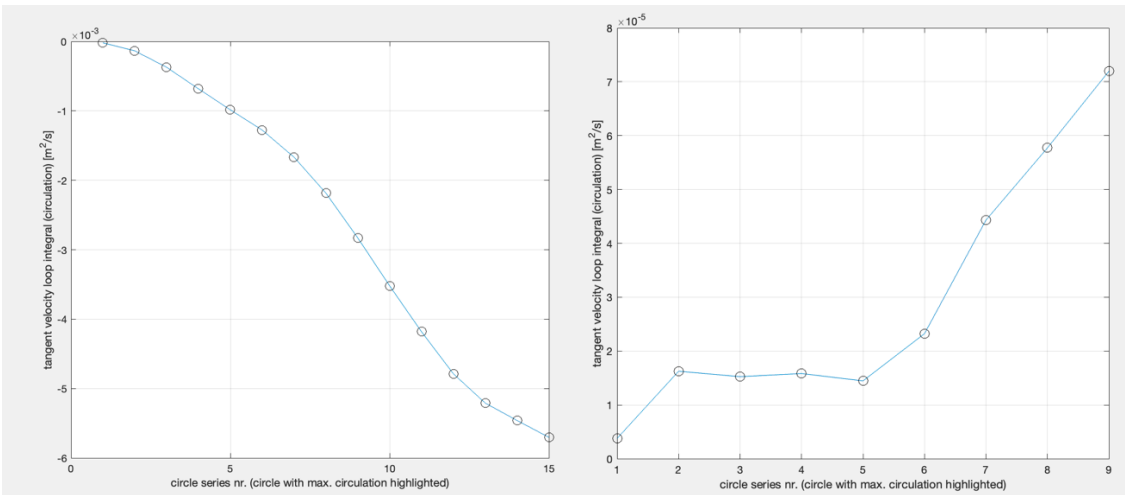


Baseline

Blended up

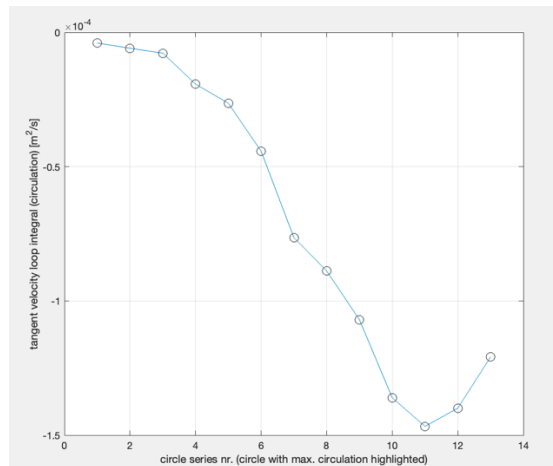


Blended down



Back curved

Double facing-top



Double facing-bottom

Table J1: Winglet Circulation at radius 3.77 mm in m²/s, ranked from highest to lowest circulation

Winglet Type (highest to lowest circulation)	Radius (mm)	Circulation (m ² /s)
Baseline	3.77	-0.00025
Double facing: (upward tip) (bottom tip) (magnitude)	3.77	0.00015
	3.77	-0.000025
	3.77	0.000148
Back-curved	3.77	-0.00010
Blended down	3.77	-0.000098
Blended up	3.77	-0.000072

Peak Vorticity (ω) & Downwash Strength:

Vorticity measures the local rotation of fluid and is a direct indicator of vortex intensity. Lower peak vorticity and a wider distribution generally indicate a weaker, more diffuse vortex, which correlates with reduced induced drag. Similarly, downwash—the downward flow induced

by wingtip vortices—also contributes to induced drag, while reduced or even upward vertical flow (upwash) can help recover energy and improve aerodynamic efficiency.

Table J2: Mean vorticity (ω) and downwash strength for each winglet design

Winglet Type	Area (m ²)	Mean Vorticity (1/s)	Mean Downwash (m/s)
Baseline	0.00025301	-2.8226	-0.0075843
Back-curved	0.00025027	-1.3943	7.6711e-05
Double facing: (upward tip) (bottom tip)	0.00021253	1.1433	-0.001082
	0.00024815	-0.50239	0.0028698
Blended up	0.00025889	-0.6028	-0.0014434
Blended down	0.00026673	-0.48349	-0.000314

Vortex Core Radius (r_c)

The vortex core radius represents the size of the vortex’s central region, where the flow rotates like a solid body. A smaller, tightly packed core is associated with higher velocity gradients and stronger induced drag, while a larger, more diffuse core spreads the rotational energy over a wider area, reducing its aerodynamic impact. Therefore, maximizing the core radius can help mitigate wingtip-induced drag. In this study, core radius was determined at the point where tangential velocity peaked—i.e., where velocity ceased to increase linearly with radial distance from the vortex center.

Table J3: Max vortex core radius in millimeters for each winglet design

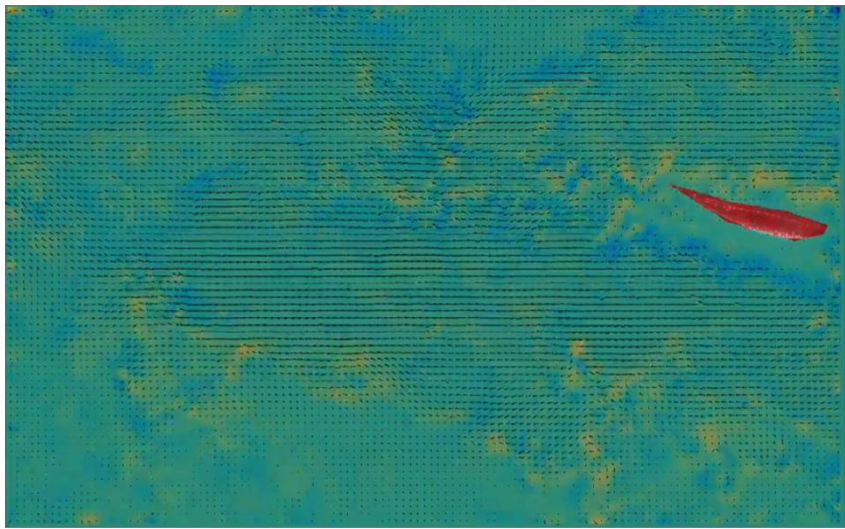
Winglet Type	Max Vortex Core Radius Circle Number	Max Vortex Core Radius (mm)
Baseline	15	11.30
Back-curved	15	11.30
Double facing: (upward tip) (bottom tip)	9	6.778
	11	8.283

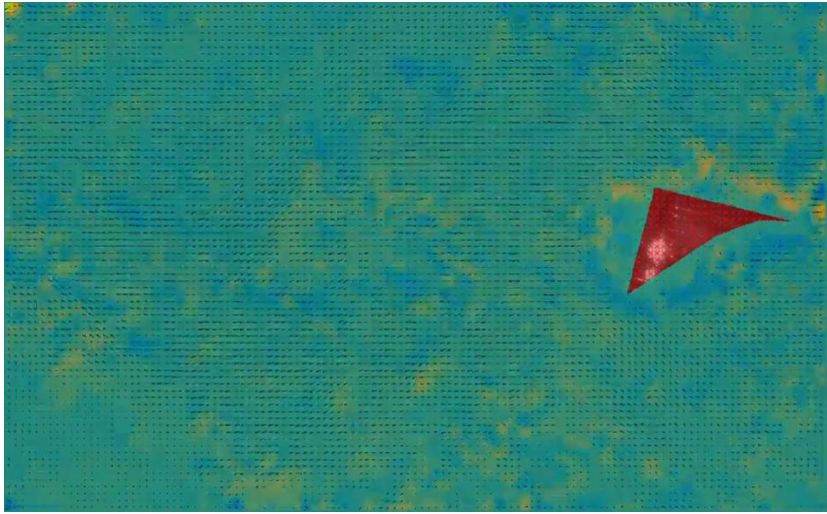
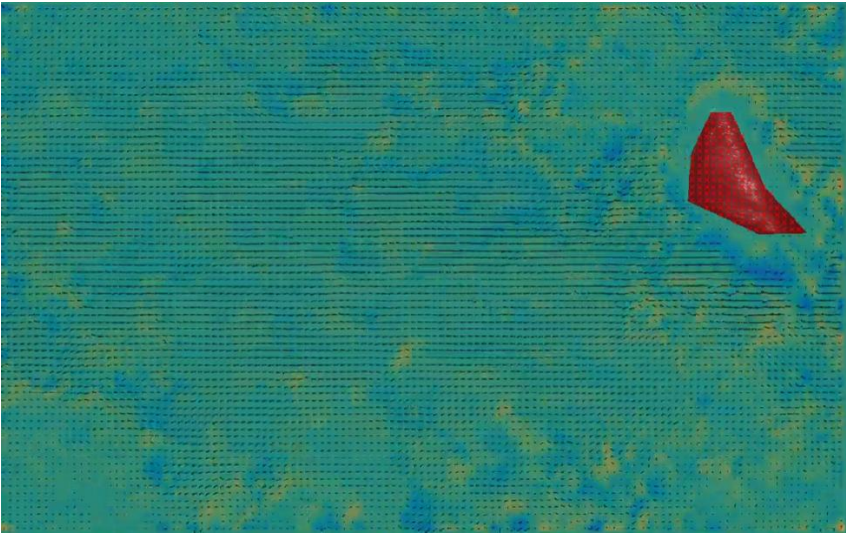
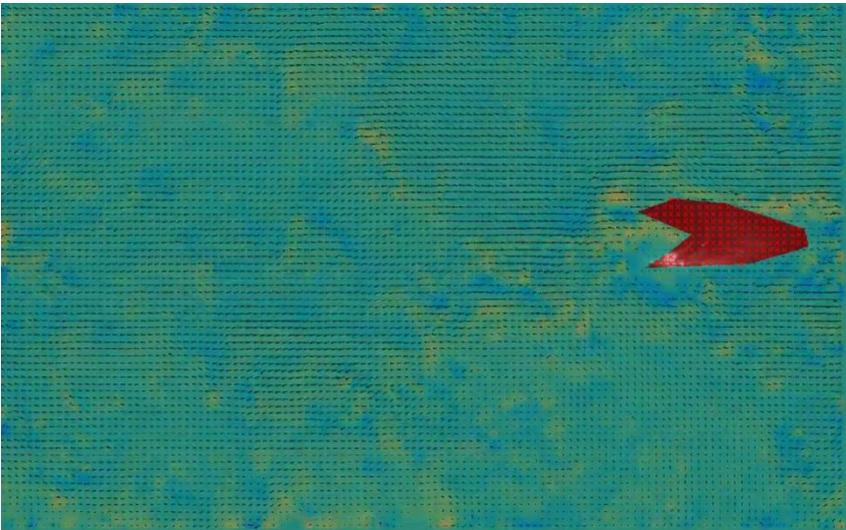
(total)	10	7.53
Blended up	10	7.53
Blended down	8	6.02

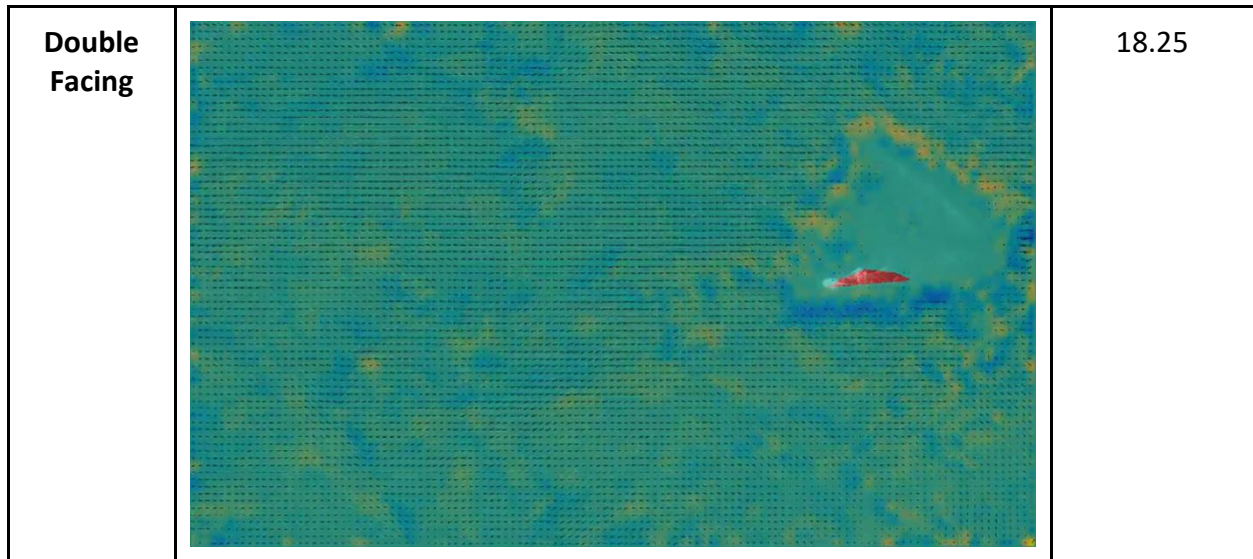
Vortex Decay Rate

The vortex decay rate can determine how efficiently a wing reduces induced drag. A higher vortex decay rate indicates that the winglet is effectively disrupting and dissipating these vortices more rapidly, which translates to improved lift-to-drag ratios and fuel efficiency. To estimate the vortex decay rate for different winglet types, vorticity animations were created using PIVlab and were analyzed with the assistance of OpenAI's ChatGPT (version from April 16, 2025), which used Python and a pixel-based intensity method. Each animation was converted to grayscale to represent vorticity magnitude, and the average vorticity was calculated across the spanwise direction to produce a 1D decay profile along the downstream flow direction. These profiles were normalized and fitted with an exponential decay function of the form $f(x)=ae^{-bx}+c$, where the decay constant b indicates how rapidly vortex strength diminishes.

Table J4: Vortex decay by wing type and constant

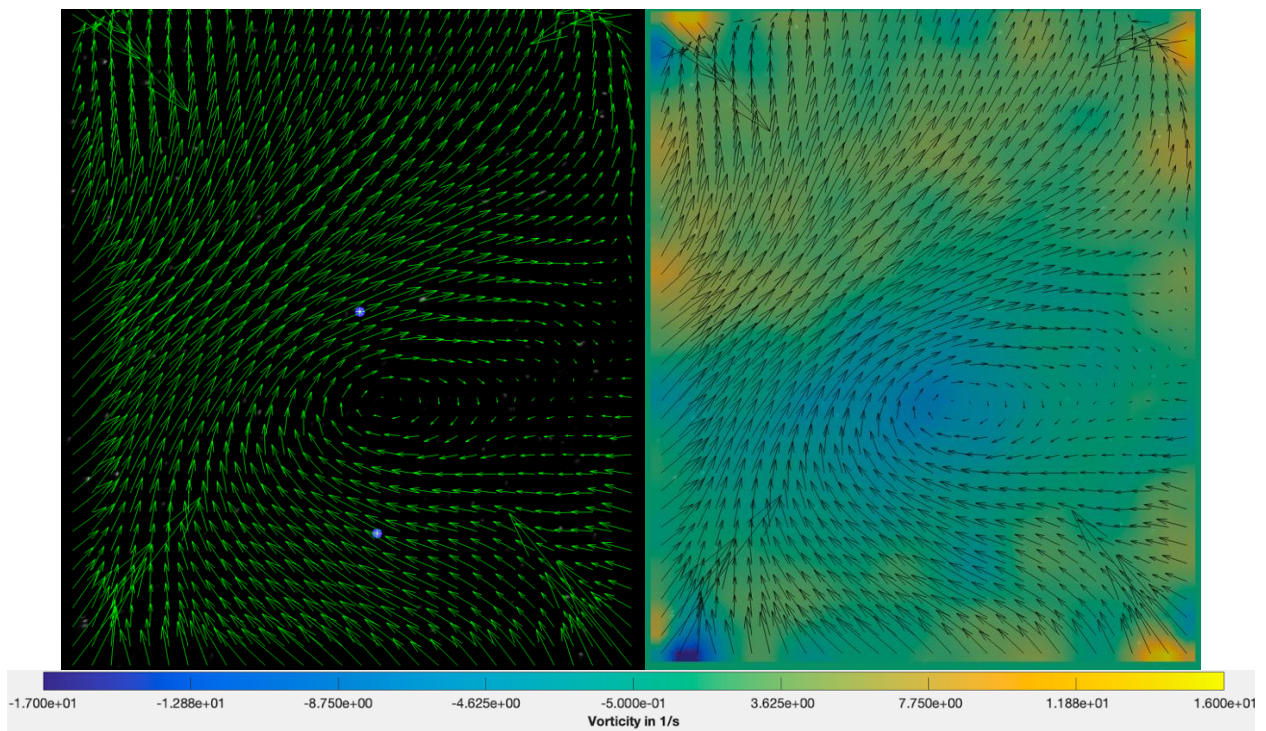
Wing Type	Picture	Decay Constant
Baseline		0.035

Blended Up	 A visualization showing a red, curved, arrow-like shape pointing upwards and to the right, set against a background of blue and green with a fine grid pattern.	22.57
Blended Down	 A visualization showing a red, curved, arrow-like shape pointing downwards and to the right, set against a background of blue and green with a fine grid pattern.	23.44
Back Curved	 A visualization showing a red, curved, arrow-like shape pointing to the right, set against a background of blue and green with a fine grid pattern.	20.83

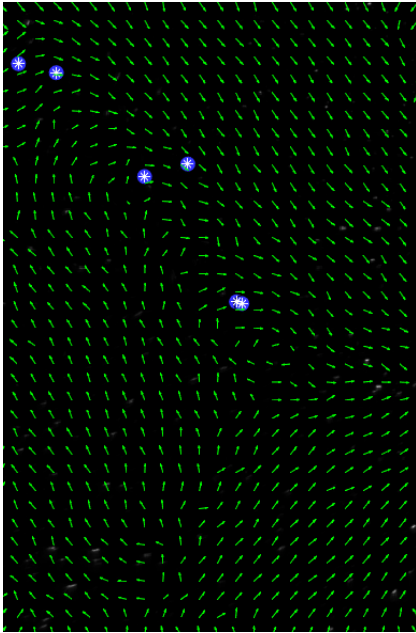


Raw Data & Images

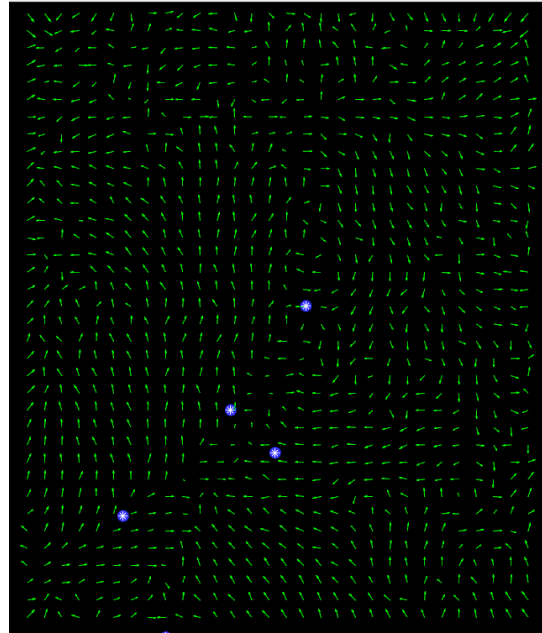
Baseline:



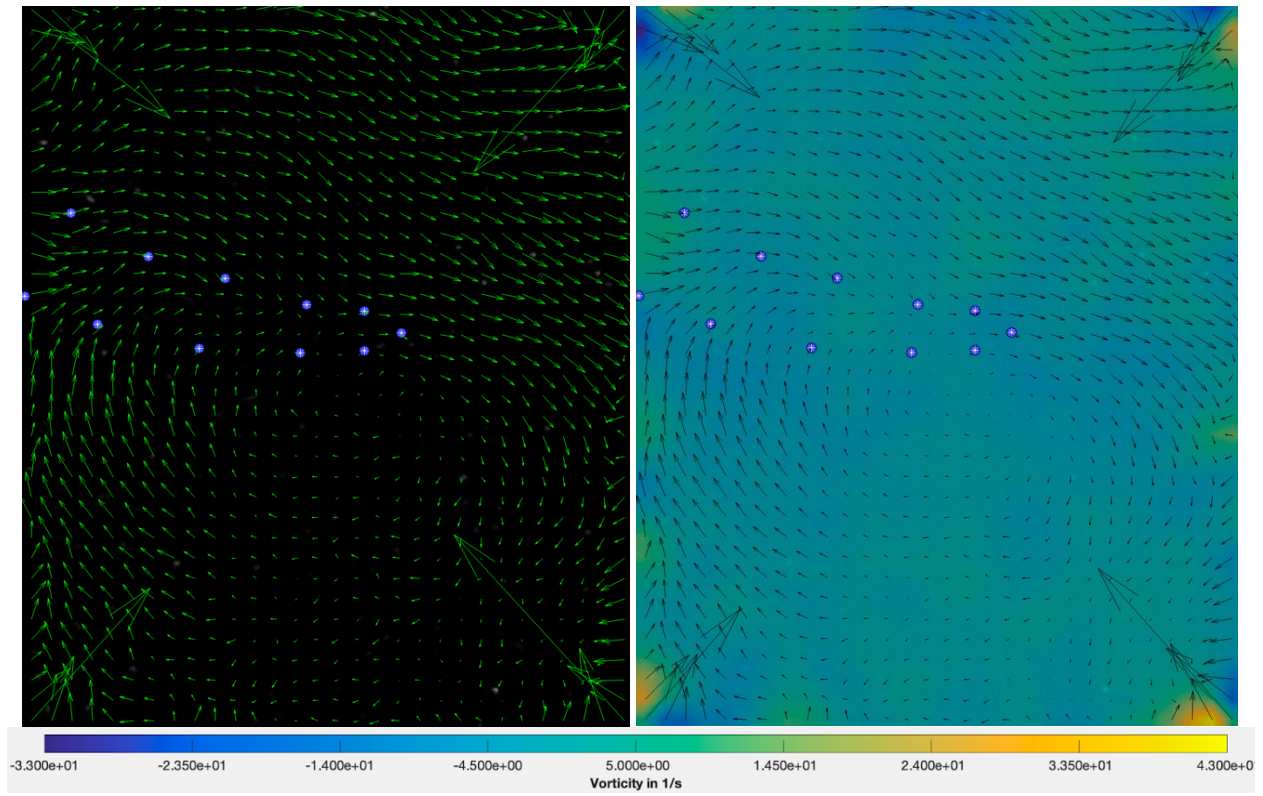
Blended up:



Blended Down:



Back Curved:



Double Facing:

